Modeling and Control of Eddy-Current Brakes

Lars Rudolfsen
Master of Science in Cybernetics and Robotics,
Norwegian University of Science and Technology,
Department of Engineering Cybernetics

Supervisor: Morten Dinhoff Pedersen, ITK

August 20. - December 18. 2018

Abstract

A review of the existing literature on the concept of contactless braking using eddy currents induced in conductive materials moving relative to a magnetic field, and the real world applications and control algorithms that take advantage of this phenomenon. The topics covered include: Analytical modeling of eddy current brake force, robust brake force control using the discontinuous control algorithm; Sliding Mode Control, optimal linear control; Linear Quadratic Regulation, digital implementation and simulation of brake force control on linear motion of a conductive aluminium sheet.

Contents

List of Figures

List of Tables

Chapter 1

Introduction

This report is a documentation of the work and literature review done by the student/author on the subject of contactless braking, and serves as the main deliverable in the subject TTK4550 - *Specialization Project* as part of the 5 year MSc programme *Cybernetics and Robotics* at NTNU Gløshaugen. Brief introduction of the structure and contents of the document, divided into five chapters:

1. **Introduction:** Preface, motivation and background theory.
2. **ECB Control:** Existing ECB control publications, sliding mode control and an idealized example.
3. **Model Extension:** Extensions to accepted approximate models, continuous sliding mode control and optimal linear control.
4. **Results and Discussion:** Simulation results of presented models and control algorithms.
5. **Conclusion**

1.1 Motivation

Electromagnetic braking has been explored as a concept for a little more than a century. Today, an ever increasing number of real world applications have had their mechanical, friction based, braking systems replaced by the *Eddy Current Brake* (ECB). Some of the favourable properties of ECBs are:

1. Better high speed braking performance, as friction brakes suffer from a fading effect when the temperature of the contact area rises.
2. Resistance to weather effects such as temperature and precipitation.
3. Longer lifespan of the braking mechanism, less wear and tear.

Exercise equipment, high speed railways and even fishing reels are just a few of the applications in which ECBs are common today.

1.2 Background

This section will establish the framework for the ECB system, and torque control of a rotating disc using such a system. This includes theoretical background of electromagnetism and the eddy current phenomenon, and a rundown of some fundamental publications that have formed a basis for the understanding and implementation of ECBs in control systems.

1.2.1 Fundamental Theory

In order to gain a deeper understanding of the topic, it is important that we familiarize ourselves with some of the fundamental properties of electromagnetism. A solid understanding of Maxwell's equations, Lenz's law and Lorentz force law are of particular importance in order to grasp the cause and effect of electromagnetic damping.

Faraday's Law of Induction (1.1), as generalized by Maxwell, states that when a magnetic field **B** is subject to change it will always be accompanied by an electric field **E** - which spatial variation is given by the rate of change in time of **B**:

$$\nabla \times \mathbf{E} = -\frac{\partial \mathbf{B}}{\partial t} \tag{1.1}$$

The opposite is also true, in that a time varying electric field will be accompanied by a spatially varying magnetic field: *Ampéres Circuital Law* (1.2), also generalized by Maxwell, describes the behaviour of the magnetic field around some flow of current. When an electric field **E** changes in time, such as when an electric current flows through a conductor, the moving charges will be accompanied by a magnetic field around the conductor:

$$\nabla \times \mathbf{B} = \mu_0(\mathbf{J} + \varepsilon_0 \frac{\partial \mathbf{E}}{\partial t}) \tag{1.2}$$

In (1.2) μ_0 and ε_0 are the permeability and permitivity of empty space, respectively. **J** is the current density in the conductor.

Lenz's Law states that when an electric current is induced in a conductor due to a change in **B**, the orientation of said current will be such that it generates a magnetic field counteracting the original change in **B**. One can see that Lenz's law and (1.1) agree, in that the spatial variation in **E** and the rate of change in time of **B** will always be opposite. Lenz's law can be seen as analogous to Newton's third law in classical mechanics.

Lorentz Force law (1.3) describes the *Lorentz force* that acts on a particle of charge q and velocity $\mathbf{v}$ due to external electric and magnetic fields:

$$\mathbf{F} = q(\mathbf{E} + \mathbf{v} \times \mathbf{B}) \tag{1.3}$$

(1.3) tells us that when some conductive material moves through an external electric or magnetic field, charged particles in the material will begin to move relative to the conductor due to the Lorentz force.

The vector form of *Ohm's Law* is a reformulation of the original result by Georg Ohm,

$$\mathbf{J} = \sigma\mathbf{E} = \frac{1}{\nu}\mathbf{E} \tag{1.4}$$

stating that the amount of current flowing through a cross sectional area $\mathbf{J}$ at any point in a material of conductivity σ (or alternatively, resistivity ν) is equal to the product of the conductivity and the electric field $\mathbf{E}$ at the given point.

1.2.2 Eddy Current

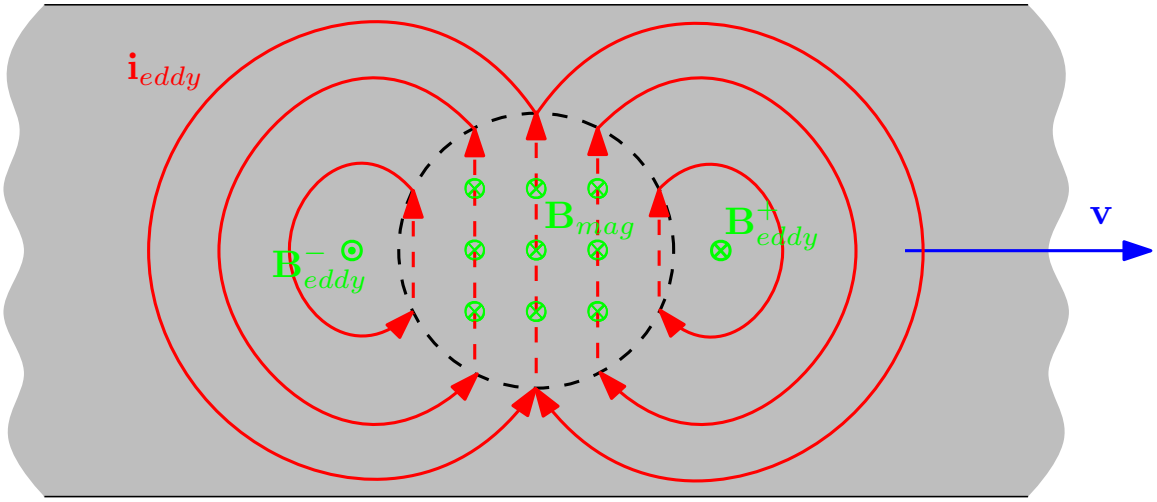

Figure 1.1: Horizontal cross sectional view of a conductive sheet moving linearly through a magnet air-gap. The circular area in the centre of the sheet is the projection of the pole area onto the sheet. Blue, green and red vectors denote the sheet velocity, induced magnetic fields and eddy current return paths, respectively.

Using the basic laws of classical electromagnetism presented in the previous section, this section will attempt to give the reader a thorough and intuitive description of the eddy current phenomenon and why it is useful to us.

When describing the phenomenon of eddy currents induced in a thin conductive sheet moving through a magnetic gap, it is useful to view the pole as split in the middle and consider what happens in the *trailing* part (the part moving into the magnetic field), and the *leading* part (the part moving out of the magnetic field) of the sheet close to the pole area. Let the sheet have instantaneous velocity $\mathbf{v}$, conductivity σ and let the magnetic field $\mathbf{B}$ be perpendicular to the sheet surface.

As the trailing part moves into the pole area, it will experience an increasing magnetic field $\mathbf{B}$. Since it is increasing, the time derivative $\frac{\partial \mathbf{B}}{\partial t}$ of this field will point in the same direction as $\mathbf{B}$. By Faraday's law of induction (1.1), a change in $\mathbf{B}$ tells us that the curl the of the electric field in the sheet will be equal to the negative time derivative of $\mathbf{B}$: $\nabla \times \mathbf{E} = -\frac{\partial \mathbf{B}}{\partial t}$. Here $\nabla \times \mathbf{E}$ is given by a vector perpendicular to the plane of the sheet, hence we know that $\mathbf{E}$ is rotating in the plane and the direction follows from the right hand rule. The same procedure for the leading half of the pole, where the magnetic field is *decreasing* in time yields the same rotation of $\mathbf{E}$ in the plane, of opposite direction. The resulting current paths

are circular and branching out of, and back into, the pole area. These return paths for the current are similar to eddy currents observed in turbulent fluids, which is where the eddy current phenomenon gets its name.

The direction of the magnetic fields induced by the eddy currents can be deduced by Lenz's law. Again, note that for the trailing part of the sheet **B** is increasing and for the leading part **B** is decreasing. Lenz's law states that a current induced by a changing magnetic field will induce a magnetic field of its own that opposes the original change. Using this fact, we know that the magnetic field induced by the eddy currents in the trailing part; $\mathbf{B}^{-}_{eddy}$ will point normal to the sheet plane, opposite to **B**. The opposing magnetic fields results in a magnetic force of repulsion between the stationary magnet and the trailing end. On the leading end, a magnetic field $\mathbf{B}^{+}_{eddy}$ with the same direction as **B** is induced, resulting in a magnetic force of attraction between the stationary magnet and the leading end. The forces on both sides of the pole area combine to oppose the direction of movement. This is the electromagnetic drag force due to eddy current induction.

1.2.3 Fundamental Literature

Maxwell [1] was one of the first to investigate the effects of induced eddy currents in a thin conductive sheet of indefinite length, moving with a velocity relative to the electromagnet. He used what is now referred to as *Maxwell's receding image construction*, to explain how the counter-magnetic field of the induced eddy currents changes over time. Roughly explained, the construction is based on a decomposition of the sheet into *positive* and *negative* parts - above and below the sheet respectively. A monopole q moves from left to right above the sheet with a velocity v. Time discretization allows for analyzing the effects of the instantaneous magnetic field of q onto the sheet at each time instant t. Maxwell's theory states that at time t, an *image* of the monopole q is created on the negative side of the sheet - these images are denoted $-q$. At the next time instant $t + \delta t$, as q moves a distance $v \cdot \delta t$ along the sheet, an image of the same strength and opposite polarity of $-q$ is created in its previous position. The imagined monopoles on the negative side of the sheet, representing the induced magnetic fields at each time-step, move away from the sheet with velocity:

$$v_0 = \frac{2}{\mu_0 \sigma d} \tag{1.5}$$

This is the *characteristic recession velocity* for a sheet with conductivity σ and thickness d. Thus, q leaves behind it a *trail of receding images* for each given time instant. Maxwell also investigated the forces applied to the moving monopole q. The drag force experienced by a monopole of strength m moving at velocity v parallel to a thin conductive sheet at distance z to the sheet was found as:

$$f_d = \frac{m^2}{4z^2} v \frac{\sqrt{v_0^2 + v^2} + v_0 - v}{(\sqrt{v_0^2 + v^2} + v_0)^2} \tag{1.6}$$

Maxwell's results are limited by the fact that they predate the discovery of the electron. Another limitation is the lack of modern computing tools, disallowing the choice of sufficiently small time steps δt in the image construction for increased accuracy. Nevertheless, Maxwell's receding image construction was used to calculate accurate drag/lift force models in several succeeding articles on the eddy current phenomena.

The theory of eddy currents in thin conductive sheets was first (successfully) extended to braking systems by Rüdenberg [2]. His results are based on a sheet of infinite length moving through an infinite series of magnetic gaps. Suppose the magnets are designed such that the magnetic field is sinusoidally alternating along the length of the sheet (Figure 1.2). Using the assumption that the eddy current distribution can be accurately described using sinusoidal functions, he obtained the formula:

$$K = \frac{1}{4} \frac{d}{s} B_1^2 v \lambda^2 \frac{w}{(vl/s)^2 + w^2} \tag{1.7}$$

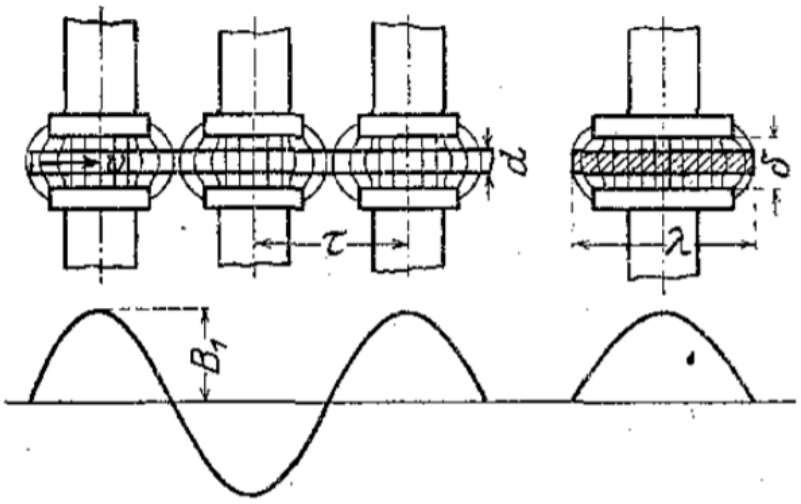

Figure 1.2: Rüdenbergs infinite sheet moving through a series of magnetic gaps with sinusoidally distributed magnetic fields with amplitude B_1. τ is the space between each pole, d is the sheet thickness, λ is the side length of the square poles, and v is the sheet velocity. Figure source: [3, p.134].

Where $K[10^{-3} \cdot \mathrm{g}]$ is the braking force for each pole. $s[\mathrm{m}^2/\mathrm{s}]$, $w[1]$ and $l[\mathrm{m}]$ are known parameters. Rüdenberg noted a decaying breaking force at high velocities. In particular, (1.7) predicts a descent in K proportional to $\frac{1}{v}$ as $v \to \infty$, and predicts the critical torque and velocity to be proportional to the magnet airgap δ.

Extensive experiments of the results and formulas proposed by the available literature on ECBs in the early 20th century were conducted by Zimmermann [3]. Conductive sheets of infinite length, which several of the relevant models were derived from, do not exist in reality. Thus, testing rigs for the ECB brake force models are typically in the form of rotating disks of some conductive material - and the measured braking torque by the ECB on them. Two different experimental configurations were used: Firstly, a *Pasqualini-brake*, consisting of a thin conductive disc rotating through two circular magnet gaps placed on opposite sides of the disc at equal distance from the center. Secondly, a *Siemens-brake*, with a thin conductive ring through polygonal magnet gaps on opposite sides. Various conductive metals, including aluminium, for the disc were also tested. Zimmermanns experimental results were a crucial source of verification for the preceding and succeeding literature on ECBs.

The Pasqualini-brake configuration was found to consistently outperform the Siemens-brake, which might explain why the former is the preferred experimental configuration in later works on ECBs. Rüdenbergs [2] brake force formula could not be verified experimentally (Figure 1.3), nor the claimed proportionality of critical velocity (and brake force)

and the magnet airgap. Zimmermann instead observed a ”slower than proportional ascent”

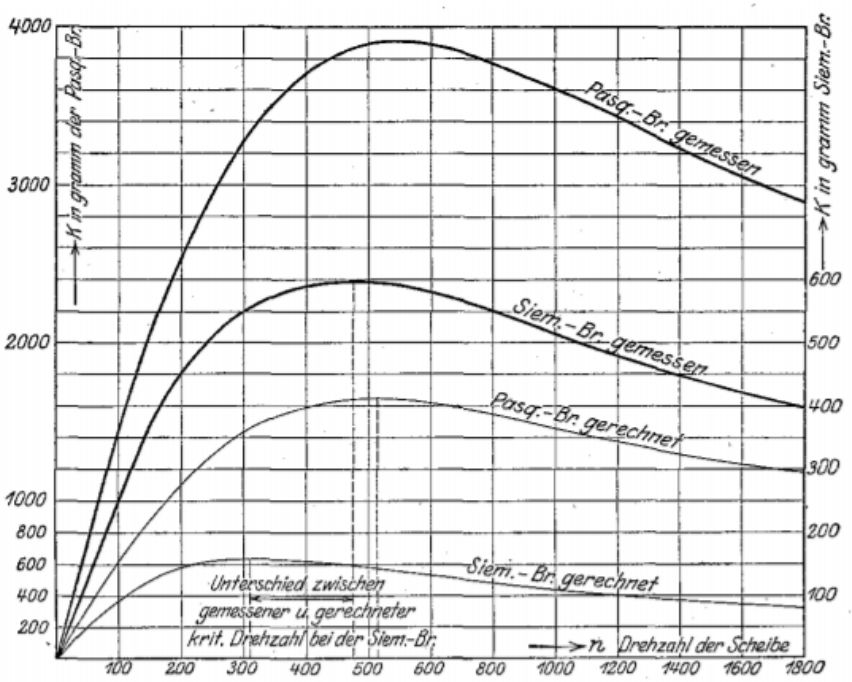

Figure 1.3: Rüdenbergs equation (1.7) (*gerechnet*; expected) compared with experimental results (*gemessen*; measured). The plot [3, p.144] shows braking force as a function of disc velocity.

of brake force as a function of magnet airgap. Experimental results (Figure 1.3) revealed that for low speeds, brake force is proportional to sheet velocity and for high speeds, brake force is proportional to the inverse velocity. Zimmermann concludes that (1.7) has some validity in predicting the ascending and descending proportionality of the brake force.

Smythe [4] and Scheiber [5] successfully expressed the induced eddy current distribution, in a thin rotating disc through circular magnet gaps, in terms of differential equations - solved analytically [4] and numerically [5] to yield agreeing expressions for the resulting braking torque:

$$T = \frac{\pi}{2\nu} R^2 \delta m^2 B^2 \omega \left[1 - \frac{(R/a)^2}{(1 - m^2/a^2)^2} \right] \tag{1.8}$$

Where $\nu = \sigma^{-1}$ is the sheet resistivity, R is the pole radius, δ is the sheet thickness, m is the pole lever arm from disc centre and a is the disc radius. (1.8) proved accurate in the linear low velocity region, but do not predict a critical velocity and braking torque. Smythe extended his method to the high speed region, but predicted a descent in brake torque steeper

than ω^{-2} for $\omega > \omega_c$ which does not agree with experimental results (Figure 1.3).

Wouterse [6] introduced the concept of an ideal eddy current brake, and proposed a formula for computing the critical velocity v_c - more accurate to experimental results [3] than the preceding literature. An ideal eddy current brake means that the return path of the induced currents follows the outline of the pole area, and is of zero resistance, as if the pole was surrounded by a superconductive ring. The result of this assumption is that the current density $\mathbf{J} = -1/\nu(\mathbf{v} \times \mathbf{B})$ of the induced electrical field $\mathbf{E} = -\mathbf{v} \times \mathbf{B}$ is confined to the volume of the sheet covered by the pole.

Instead of describing the eddy current distribution in the sheet and solving the differential equations, as done in detail by Smythe [4] and Scheiber [5], Wouterses braking force model is based on the kinetic energy dissipated as heat in the sheet. The total power dissipation in the sheet volume under the pole, and the resulting drag force, are given by:

$$P_{diss} = \int_V \nu J^2 dV = \frac{\pi}{4\nu} D^2 d B^2 v^2 \tag{1.9a}$$

$$F_e = \frac{P_d}{v} = \frac{\pi}{4\nu} D^2 d B^2 v \tag{1.9b}$$

Where ν is the resistivity of the sheet material, D is the pole area diameter, d is the sheet thickness, B is the external magnetic field acting on the sheet, and v is the sheet velocity. At low speeds the magnetic brake behaves as a linear damper, as B does not deviate significantly [6, p. 154] from the initial magnetic field B_0 for $v << v_c$. Wouterse includes the factor c

$$c = \frac{1}{2}\left[1 - \frac{1}{4}\frac{1}{(1+\frac{R}{A})^2(\frac{A-R}{D})^2}\right] \tag{1.10}$$

in (1.9) to compensate for the fact that in real systems, the return path of the eddy currents is not of zero resistance. In (1.10), R is the lever arm of the pole from the disc center, and A is the disc radius. This yields the drag force expression

$$F_e = \frac{\pi}{4\nu} D^2 d B_0^2 c v \tag{1.11}$$

which agrees with the initial results of Smythe [4] and Scheiber [5] (1.8).

Wouterse's critical velocity formula:

$$v_c = \frac{2}{\mu_0}\sqrt{\frac{1}{c\xi}} \cdot \frac{\nu}{d}\sqrt{\frac{x}{D}} \tag{1.12}$$

Where x is the airgap length, including sheet thickness, and $\xi \approx 1$ is a proportionality factor. Wouterse's results, though not completely accurate to reality, form a good basis for initial investigations of ECBs due to their simplicity.

Chapter 2

ECB Control

The sections contained in this chapter present existing literature on real time control implementations of the models, a description of a particularly applicable control algorithm in *Sliding Mode Control*, and application of a primitive such controller to an idealized brake force model.

It is tempting to apply the ECB to the speed dynamics of some vessel, and indeed - most of the literature on the topic of ECB control investigates ECB performance in speed regulation. However, use of approximate brake force models will serve as one of several sources of error in such applications. For this reason we will focus on control of the one-dimensional braking torque/force output of the ECB itself. While the system representing the magnetic field density is characterized by the classically well behaved (under certain conditions), linear relation $B \propto i$ - output reference control of the braking force/torque is less straight forward.

Complications in controller implementations of the ECB arise from the nonlinearity in the braking force output, ubiquitous to accepted analytical models (Section 1.2.3): $F_{ECB} \propto B^2$. The brake force dynamics of an ECB generally takes the form:

$$\begin{aligned} \dot{x}(t) &= a(t)x(t) + b(t)u(t) \\ y &= c(t)x(t)^2 \end{aligned}$$

The lack of a sufficiently accurate, stationary brake force model has motivated the use of robust and/or adaptive control algorithms to counter the uncertainty of the system parameters, particularly in the brake force model parameter $c(t)$.

2.1 Existing Literature

Optimal torque control of an ECB mechanism on the wheel(s) of ground vehicles where the minimized objective is the braking distance was investigated by Kapjin Lee and Kyihwan Park [7], followed by Sohel Anwar and Bing Zheng [8]. Due to the many advantages of ECBs compared to friction brakes, some of which have already been mentioned (Section 1.1), these publications investigate the use of ECBs in *Anti-lock Braking Systems* (ABS) applications. A publication by Jeonghoon Song [9] also investigates the use of ECB for control of the angular motion of rotating disks, and proposes a hybrid hydraulic-ECB - citing low braking force output of the ECB at low speeds. [7–9] share a similar approach to ECB control, using variants of (1.11) as approximate braking force models and discontinuous control algorithms (sliding mode control). Good reference torque tracking is consistent for each of the three publications, as well as performance issues associated with the control algorithm.

On the other hand, E. Simeu and D. Georges [10] successfully designed and implemented a continuous linearizing control algorithm based on a modification of (1.11) to include magnetic hysteresis, which combined with state/parameter estimation yielded quite good experimental results while bypassing the drawbacks of the discontinuous controller used by [7–9].

Linear motion braking force control was investigated by R. Hong-Je et al. [11]. 2D *Finite Element Method* (FEM) was used instead of approximate models for the brake force, and near constant brake force control was achieved experimentally using only a linear feedback controller (PI).

2.2 Sliding Mode Control

An alternative to numerical solutions of a complex system, is an approximate model accompanied by a robust control algorithm capable of effectively eliminating uncertainties in finite time. This approach is often preferred in early stages of modeling and control due to its reliability and comparably simple implementation. One such algorithm popular for electro-mechanical systems is the *Sliding Mode Controller* (SMC).

Sliding mode control is a discontinuous control algorithm that, by defining the input as $\mathbf{u} = -M\boldsymbol{\sigma}(\mathbf{s})$, forces the system to follow a *sliding surface* from both sides. To achieve this, M is set as a very high gain - typically given by the maximum output of the actuator. $\boldsymbol{\sigma} : \Re^m \rightarrow \{-1, 0, 1\}^m$ is a discontinuous function, typically chosen as $\boldsymbol{\sigma}(\mathbf{s}) = \text{sgn}(\mathbf{s})$. Consider the nonlinear time varying state-space:

$$\dot{\mathbf{x}} = \mathbf{f}(\mathbf{x}, \mathbf{u}, t) \ , \quad \mathbf{x} \in \Re^n$$
$$\mathbf{u} = -M\text{sgn}\{\mathbf{s(x)}\} \ , \quad M > 0 \ , \quad \mathbf{s} \in \Re^m$$

Where $m \leq n$ and $\mathbf{s(x)} = \mathbf{0}$ defines m sliding surfaces. The system is said to be in *sliding mode* when it is "sliding" across the sliding surface(s) given by $\mathbf{s} = \mathbf{0}$ for a first order SMC. In general, the sliding mode for a p-order SMC is given by $\mathbf{s} = \dot{\mathbf{s}} = ... = \mathbf{s}^{(p-1)} = \mathbf{0}$ [12]. We wish to express $\mathbf{s}(\mathbf{x}) = \mathbf{0}$ in terms of wanted behaviour of the nonlinear system. One example of this could be $\mathbf{s} = \dot{\mathbf{x}} + c\mathbf{x}$, where $c > 0$ [13]. The sliding mode of the system is then given by the dynamics $\dot{\mathbf{x}} = -c\mathbf{x}$, which has an asymptotically stable equilibrium point at $\mathbf{x} = \mathbf{0}$. SMCs are characteristically robust, as the feedback gain (if chosen large enough) will overpower the effect of any uncertainties in the plant model.

One cannot blindly define desired system behaviour as a sliding surface however, as the sliding surface must be *reachable*. The *reachability conditions* of a SMC are the conditions at which the solutions $\mathbf{x}(t)$ reach the sliding surface in finite time. Reachability conditions are not uniquely defined in the literature on SMC, using the η-reachability condition [12]:

$$s_i \dot{s}_i < -\eta |s_i|, \ i \in \{1, 2, ..., m\}, \ \forall \ \mathbf{s}, \dot{\mathbf{s}} \in \Re^m / \{\mathbf{0}\} \tag{2.1}$$

Where $\eta > 0$ is some arbitrarily small design parameter.

SMCs are particularly well suited towards electromechanical systems, as they often use transistors as actuators that naturally produce a high frequency switching output. In such cases, discontinuous control algorithms such as SMC are often favored over continuous control schemes with Pulse-width Modulation (PWM) [13].

A significant drawback of the SMC algorithm, is the sliding mode behaviour of switching around $\mathbf{s} = \mathbf{0}$ at an infinitely large frequency. As this is obviously not possible in practice due to physical limitations of actuators, sliding mode controllers give rise to a *chattering* effect (high frequency oscillations) around the sliding surface. This effect is often exacerbated by the presence of unmodeled dynamics, that due to the high gain may become significant. In practice, some approximation of the discontinuous function $\boldsymbol{\sigma}$ must be used in the implementation - which can greatly reduce chattering depending on the approximation used. Higher order SMC implementations are also effective in reducing chattering. Implementing observers has also shown to effectively filter out the high frequency components of the sliding mode controller [13]. These methods all come with drawbacks, one example being that control systems using approximations of the discontinuous control signal typically converge to a nonzero error. The error is greater depending on the accuracy of the approximation.

2.3 Example

Symbol	Description	Value
d	Sheet thickness	5mm
D	Magnet pole diameter	10mm
l_g	Air-gap length	5mm
l_c	Magnet core length	20cm
μ_0	Vacuum permeability	$4\pi \cdot 10^{-7}\text{H/m}$
μ_c	Magnet core permeability (iron 99.8% pure)	$6.3 \cdot 10^{-3}\text{H/m}$
μ_d	Sheet permeability (aluminium)	$\approx 4\pi \cdot 10^{-7}\text{H/m}$
R_{mag}	Electromagnetic circuit resistance	2.1Ω
N	Number of inductor turns around magnet core	1200
σ	Sheet conductivity (aluminium)	$2.0202 \cdot 10^{7}\text{S/m}$
ν	Sheet resistivity (aluminium)	$0.0495 \cdot 10^{-6}\Omega\text{m}$
c	Brake force model compensation factor	0.5

Table 2.1: Physical parameter values used for all simulations in this report.

To gain a better understanding of the basics of electromagnetic braking systems, as well as their response to sliding mode controllers, consider the following example of a linear brake controlled by a first order sliding mode controller. The system is considered in its simplest form to highlight the performance of the ECB under ideal circumstances.

Assume a thin sheet of thickness d and conductivity σ and of indefinite length is placed under an electromagnetic pole with airgap l_g, exciting a stationary and uniformly distributed magnetic field **B** of magnitude B_0 through the plane of the sheet (Figure 2.1). Now let the sheet move with velocity **v** and speed v relative to the pole. As explained in Section 1.2.2, the sheet will experience a drag force caused by the magnetic fields of the induced eddy currents on the sheet. Our objective is to control this electromagnetic drag force F_e (1.11) to a reference force F_r using a sliding mode controller. For the described configuration, the compensation factor (1.10) is $c = 0.5$

2.3.1 Modelling the electromagnet

The magnetic field **B** is generated by a simple RL-circuit (Figure 2.2). We will control the strength of the magnetic field by using the command voltage V_{cmd} as our input. Kirchoff's

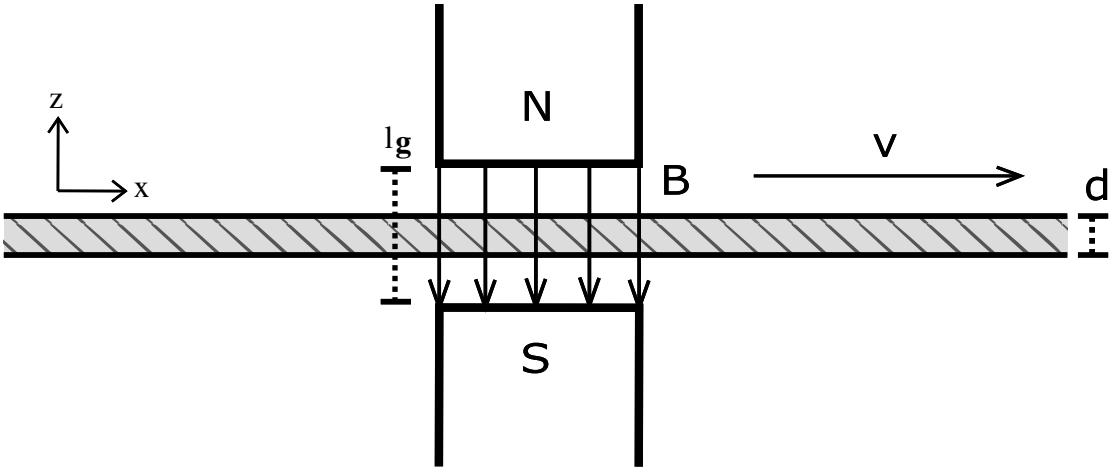

Figure 2.1: xz-plane of the infinite sheet moving through the magnetic field B.

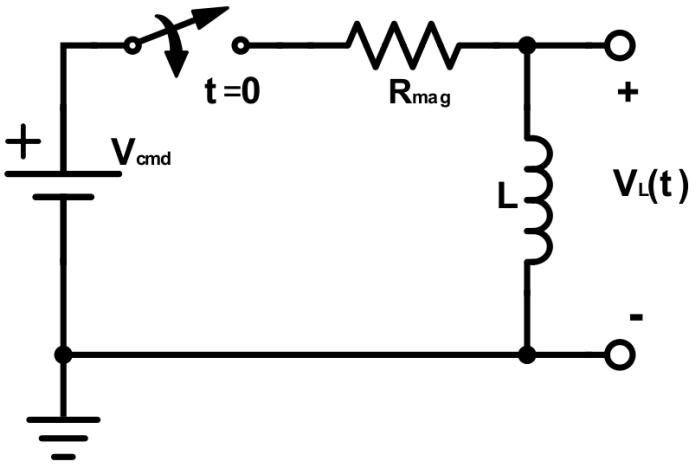

Figure 2.2: Circuit model of the electromagnet. $V_{cmd}[\mathrm{V}]$ is the command voltage generated by the controller. $R_{mag}[\Omega]$ is the resistance of the electromagnet circuit. The inductor has inductance $L[10^{-3} \cdot \mathrm{H}]$ and has N windings around a metal core of permeability $\mu_c[\frac{\mathrm{H}}{\mathrm{m}}]$. $V_L(t)$ is the voltage over the inductor at time t.

voltage law yields the differential equation:

$$\frac{\mathrm{d}}{\mathrm{dt}}i(t) = \frac{1}{L}(-R_{mag}i(t) + V_{cmd}) \tag{2.2}$$

The time-constant of which is given by:

$$\tau_{RL} = \frac{L}{R_{mag}} \tag{2.3}$$

Inductance L of the differential equation (2.2) can be calculated as:

$$L = \frac{\mu_0 N^2 A_c}{l_c} \tag{2.4}$$

Where A_c and l_c are the cross-sectional area and length of the core, respectively.

An idealized electromagnetic model will be used to express B_0. The magnetomotive force, induced by the current i passing through the inductor with N windings around a permeable core, is given by $\mathcal{F} = Ni$. Magnetic flux through the core can be computed as $\phi = \frac{\mathcal{F}}{\mathcal{R}}$ where $\mathcal{R}$ is the total reluctance. Reluctances in the core, airgap, and disc are given in series by:

$$\mathcal{R}_c = \frac{l_c}{\mu_c A_c}$$
$$\mathcal{R}_g = \frac{l_g - d}{\mu_g A_g}$$
$$\mathcal{R}_d = \frac{d}{\mu_d A_d}$$

Where l_i, μ_i, A_i are the length, permeability and cross-sectional area, and d is sheet thickness. We assume no fringing in **B**, so that $A_g = A_d = A_c$. We also assume that the permeabilities of air, the disc, and the core are equal to the vacuum permeability μ_0. The magnetic field, or magnetic flux density in the gap is then given by:

$$B_0 = \frac{\phi}{A_g} = \frac{\mu_0 N i}{l_c + l_g} \tag{2.5}$$

If we assume that $\mu_c >> \mu_0$, as is the case for most non air cores, the magnetic flux density simplifies to

$$B_0 = \frac{\mu_0 N i}{l_g} \tag{2.6}$$

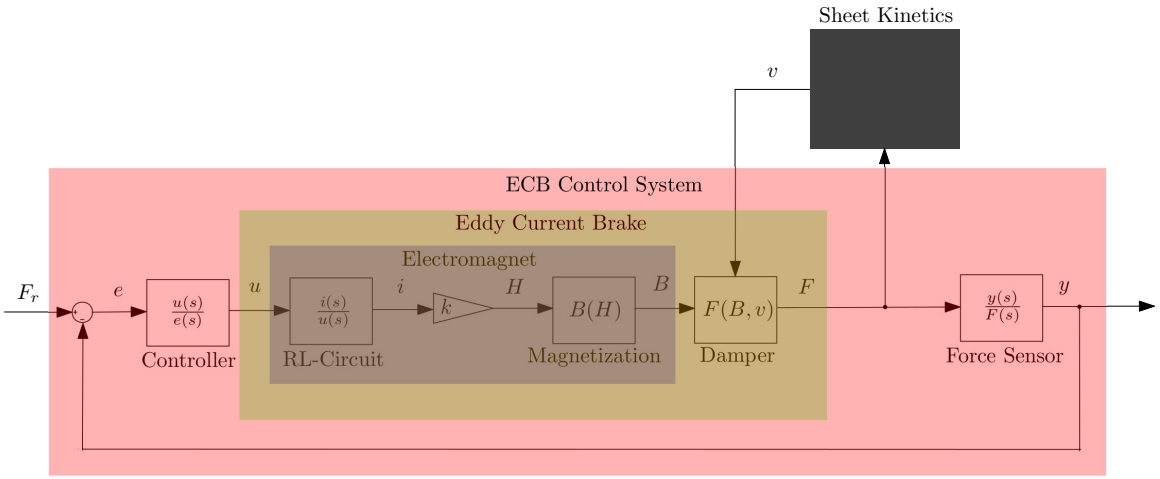

Figure 2.3: Architecture of ECB control systems referred to throughout this paper.

2.3.2 Controller Design

Consider the system architecture (Figure 2.3). We choose to design the control input $u = V_{cmd}$ of the electromagnet actuator as a primitive sliding mode controller: The simplest form of a first order sliding mode controller is given by the sliding surface defined by the tracking error: $s = e = F_r - F_e = 0$. Since our model (1.11) depends not on B_0, but on B_0^2, a traditional SMC design $V_{cmd} = -V_{max}\text{sgn}(s)$ will fail to make our system slide along $s = F_r - F_e = 0$. In physical terms, the inputs $V_{cmd} = \{-V_{max},\ V_{max}\}$ will push F_e in the same direction since they only serve to reverse the polarity of **B** which will produce a drag force of the same magnitude and direction. For this reason we must modify either the sliding surface, or the controller $u = V_{cmd}$ to yield desired results. The following simulation results are based on sliding surface $s = F_r - F_e = 0$ and an "on/off" controller:

$$V_{cmd} = V_{max}\theta(s) \begin{cases} V_{max} & s > 0 \\ \frac{1}{2}V_{max} & s = 0 \\ 0 & s < 0 \end{cases} \tag{2.7}$$

Where θ is the Heaviside function. In practice, we are controlling the switch in (Figure 2.2) while the source is at a constant maximum voltage.

2.3.3 Simulations and Results

All simulations mentioned in this subsection were executed with $v(t)$ as an external variable expressed as a ramp function plateauing at $v = 4.0\text{m/s}$ at $t = 1.0$ s. The maximum

command voltage (2.7) was set to $V_{max} = 100 \cdot 10^6$ V. Note that extremely high voltage (and current) is needed to generate a sufficiently strong magnetic flux density B_0, this due to our modeling of the magnet as an air core (μ_c=μ_0).

The reference braking force was set to $F_r = 0.5$ N for all simulations, except one used to examine the sliding properties for a time varying reference. A time delay $e^{-\tau_d s}$ was included in the transfer function from F_e to F_r: $F_e(s)/F_r(s) = H(s)e^{-\tau_d s}$ with $\tau_d = 0.25$ s. The only other time constant in the system would otherwise be given by the current dynamics in the inductor (2.3), $\tau_{RL} = L/R_{mag} << \tau_d$. This was done as a measure to limit the response time of F_e, simulating reality by including the time constant of a force sensor in a physical system.

Various approximations of the discontinuous part of the controller (2.7) were tested (Figure 2.4), including a relay switching approach (Figure 2.5), a piecewise linear approximation (Figure 2.6) and a smooth (logistic) approximation (Figure 2.7).

Relay:
$$V_{cmd} = \begin{cases} V_{max} & s > q \\ [V_{max}, 0] & |s| < q \\ 0 & s < -q \end{cases}$$

Piecewise linear:
$$V_{cmd} = \begin{cases} V_{max} & s > p \\ V_{max}(\frac{1}{2} + \frac{1}{2p}s) & |s| < p \\ 0 & s < -p \end{cases}$$

Smooth (logistic):
$$V_{cmd} = V_{max}\{\frac{1}{2} + \frac{1}{2}\tanh(ks)\}$$

Where q, p, k are sharpness parameters, determining how sharply each function turns at $s = 0$. The sharper the turn, the closer the given function is to the discontinuous function $\theta(s)$. Results presented in this subsection were obtained with parameters $q = p = 0.002$, $k = 100$.

Simulation attempts of the system using the discontinuous controller (2.7) as is, did not progress as soon as the sliding mode began. This was caused by chattering of frequency approaching infinity, due to variable-step solver being used for the simulation instead of a fixed-step solver.

The step response of the relay switch controller seems to follow its reference fairly well, however: A high frequency chattering effect as discussed in (2.2) is apparent. These ef-

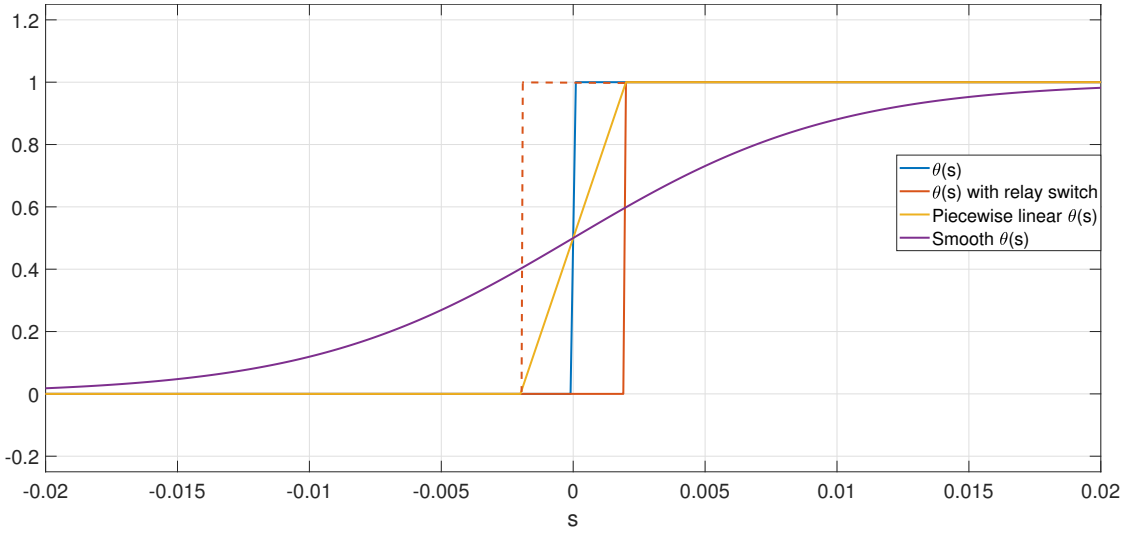

Figure 2.4: Various approximations of the Heaviside-function θ.

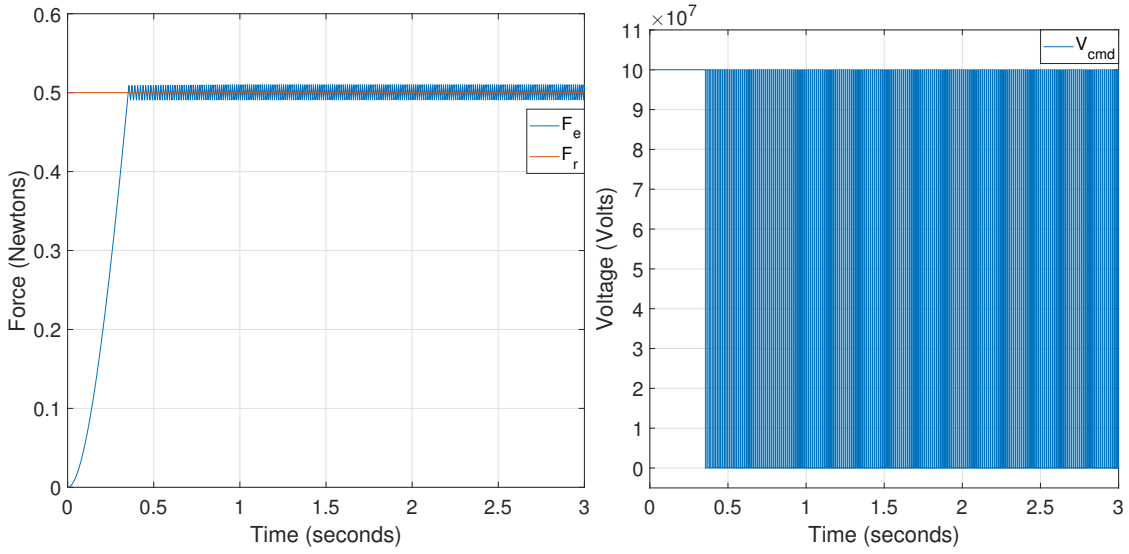

Figure 2.5: Step response of the braking force system with relay switching approximating θ.

fects are not unexpected as the relay function, despite its switching threshold limiting the chattering frequency, is still discontinuous.

Piecewise approximation of $\theta(s)$ yields a trajectory of F_r seemingly free from chattering

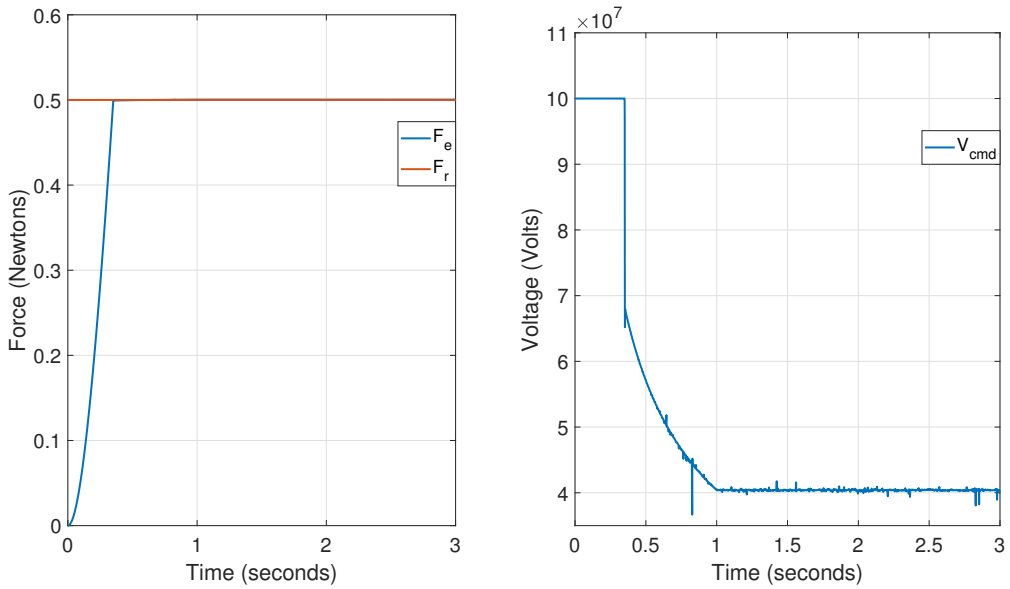

Figure 2.6: Step response of the braking force system with a piecewise linear approximation of θ.

effects, while still converging to the reference signal. The sharpness of our approximation however results in some spikes and chattering in the command voltage.

Slightly worsened trajectory for the braking force was observed for the smooth approximation of $\theta(s)$, but as expected (for a sufficiently small k) produced a command voltage free of chattering. It is important to note that the command voltage time-series produced by the last two simulations cannot be produced by a discontinuous actuator such as a transistor. We would need to control the source voltage or use a PWM of the control signal, which partly defeats the purpose of the SMC design.

The measures taken to approximate θ have successfully removed the chattering effects of the sliding mode, and have not been detrimental to the performance. Hence, there is no immediate need to implement higher order sliding modes, observers or other methods to decrease chattering for this system. Since there are no unmodeled uncertainties in this idealized example, the robustness of SMCs has not been demonstrated by these results - although: In practice, if our gain V_{max} is not too limited and sliding surfaces are properly

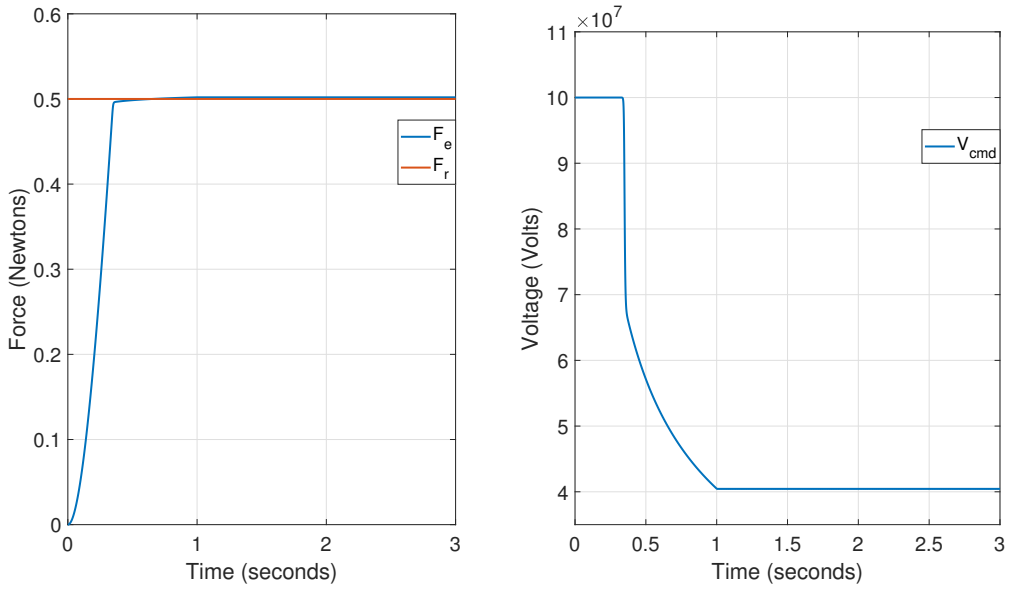

Figure 2.7: Step response of the braking force system with a smooth approximation of θ.

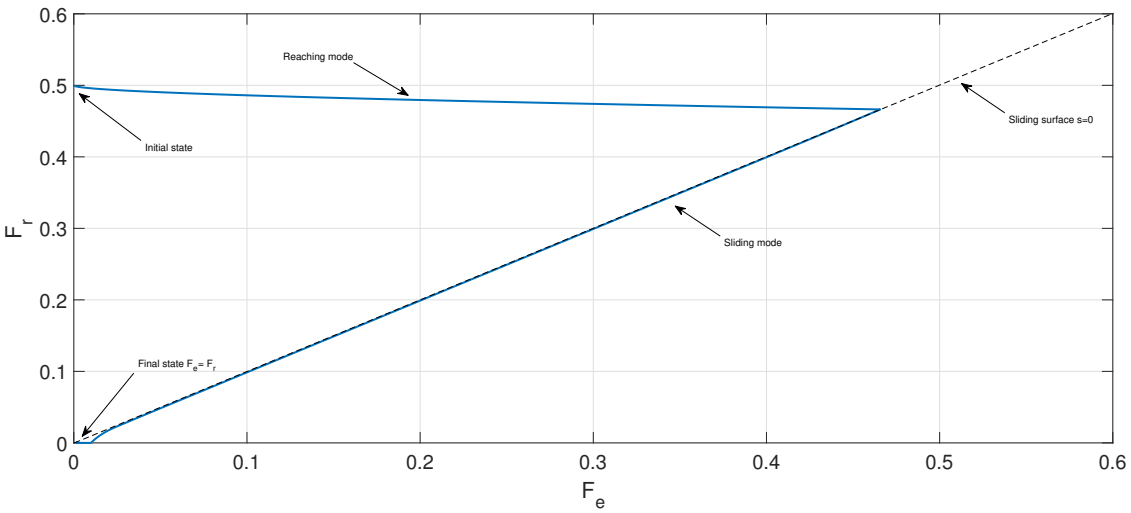

Figure 2.8: Reaching and sliding modes of the system with time varying reference signal $F_r(t)$.

defined, similar performance is expected regardless of the level of uncertainty in the system parameters. As a final point about the results, we can see that the control laws without discontinuous switching have a small stationary deviation. As mentioned in the section about SMCs (Section 2.2), this is a common drawback of using this method to suppress chattering effects. Other methods will therefore be explored in the succeeding chapter.

A simulation with a time varying reference signal $F_r(t)$ as a negative ramp starting at $F_r = 0.5$ N and saturating at $F_r = 0$ N was executed . The resulting phase plot (Figure 2.8) of ($F_e(t)$,$F_r(t)$) provides a visual representation of the *reaching mode* - when the system is being pushed toward the sliding surface from either direction, and the sliding mode.

Chapter 3

Nonlinear Model Extensions

Having successfully implemented Wouterse's brake force model (1.11) and a first order sliding mode controller, it is time to discuss the validity of the results. A good place to start is the assumptions they are based on. In order of significance, some of these assumptions are:

1. Linear damper: Speed constrained to low the "low" region, making the linear damper an accurate brake force model.
2. Zero remanence: No magnetic memory effects in the electromagnet, so that the magnetic field density in the airgap can be switched on/off with the current.
3. Assumptions not investigated in this paper:
   (a) Skin effects: The assumption that the width of the sheet d is small enough such that $d_{skin} \not< d$. That is, eddy currents are not confined to a smaller volume of the sheet of width d_{skin} which would imply non-uniform distribution of eddy currents in the material.
   (b) Energy dissipation: That all kinetic energy dissipation due to induced eddy currents is in the form of heat.
   (c) Other assumptions such as no *fringing* of the magnetic field in the airgap, affecting shape and size of the pole area on the sheet, and the notion of eddy current return paths following a superconducting ring. These factors are partly accounted for with the introduction of compensation factors (1.10).

3.1 High Speed Region

The most significant assumption made, is that the sheet velocity is constrained to small values - such that the drag force F_D can be accurately modelled as a linear damper (1.11). Many real world applications for ECBs are constrained to the low speed region, and a simplified model is often sufficient. For high speed applications, however, we must consider the following: For large v, a significant demagnetization of the external magnetic field **B** occurs, as noted by [3, 4, 6]. The demagnetization of **B**, particularly its z-component (perpendicular to the sheet), results in a decaying drag force. Experimental results (Figure 1.3) show a descent in F_D proportional to v^{-1} for $v > v_c$ when the magnetic field is induced by a constant voltage. This section includes an investigation into existing identifications of the magnetic field as a function of sheet speed,

$$B(v) = B_0 f(v)$$

and an assessment of their accuracy and performance in a drag force control application.

3.1.1 Relevant Literature

The demagnetizing effect is caused by the fact that as the conductive sheet moves through the pole at large speeds, the magnitude of the induced eddy currents and corresponding magnetic field $\mathbf{B}'$ increase to the point that $|\mathbf{B}| >> |\mathbf{B}'|$ does not hold. Since $\mathbf{B}'$ in the trailing part of the sheet has the opposite direction of **B**, it will then partly annihilate the external magnetic field. Wouterse [6] showed that as $v \to \infty$, the magnetic field induced by the eddy currents will effectively cancel out the z-component of the external magnetic field - resulting in a net zero drag force exerted. We wish to extend Wouterse's idealized model (1.11) to account for this effect.

Davis and Reitz [14] applied, and in part corrected, the method of Sommerfeld [15] to calculate an analytical drag force model including both low and high speed dynamics. Their results are based on a moving monopole q a distance over a conductive sheet, and a *receding image construction* - similar to that of Maxwell [1]. The rate at which eddy currents decay in the conducting sheet was found using Maxwells equations (1.1) and (1.2), revealing a characteristic recession velocity:

$$w = \frac{2}{\mu_0 \sigma d} \tag{3.1}$$

Where d is the sheet thickness. This agrees with Maxwell's initial result (1.5) for infinite sheets. A Riemann double-space was used to express the sheets "negative" side, where

imagined monopoles $-q$ recede from the sheet surface with velocity w (3.1), to yield an expression for the lift and drag force experienced by the monopole q:

$$F_L = \frac{\mu_0 q^2}{16\pi z_0^2}\left(1 - \frac{w}{(v^2+w^2)^{1/2}}\right) \tag{3.2a}$$

$$F_D = \frac{w}{v}F_L \tag{3.2b}$$

Where z_0 is the elevation of the monopole over the sheet surface and q is the monopole strength.

In general, drag force models based on analytic models of eddy current return paths [4, 5, 14, 16] fail to correctly identify the critical velocity of experimental torque-speed curves [17, p. 93], even if they are asymptotically accurate in low/high speed regions. This is in part caused by the large amount of heat generated in the conductive material, which can significantly change the resistance of the return paths due to material conductivity depending on temperature, while most analytical models assume constant conductivity (and resistivity). Conductivity was found by [18] to significantly impact critical braking force. Another factor is non-uniform distribution of eddy currents due to skin effects. Both of these factors becoming increasingly significant for high speed (and large eddy currents). For this reason, More recent publications [17, 18] have moved away from analytical modeling to 3D FEM analysis of the magnetic field in the air-gap.

3.1.2 Implementation

Linearity of F_D at low speeds is well documented by both theoretical [2, 4–6] and experimental results [3]. The nonlinear model (3.2) was therefore fitted to the linear model (1.11) such that they coincide in the low speed region. Taylor series expansion of (3.2) about $v = 0$ yields the linear approximation:

$$F_D = \frac{\mu_0 q^2}{16\pi z_0^2}\left(\frac{w-\sqrt{w^2}}{v} + \frac{v}{2\sqrt{w^2}} + O(v^2)\right) \approx \frac{\mu_0 q^2}{16\pi z_0^2}\frac{v}{2w} \tag{3.3}$$

Matching coefficients of the linear approximation (3.3) and the linear model (1.11):

$$q = \pm\frac{4\pi B_0\sqrt{c}Dz_0}{\mu_0}$$

Which yields the fitted model:

$$F_D = \frac{\pi c D^2}{\mu_0}B_0^2\frac{w}{v}\left(1 - \frac{w}{(v^2+w^2)^{1/2}}\right) \tag{3.4}$$

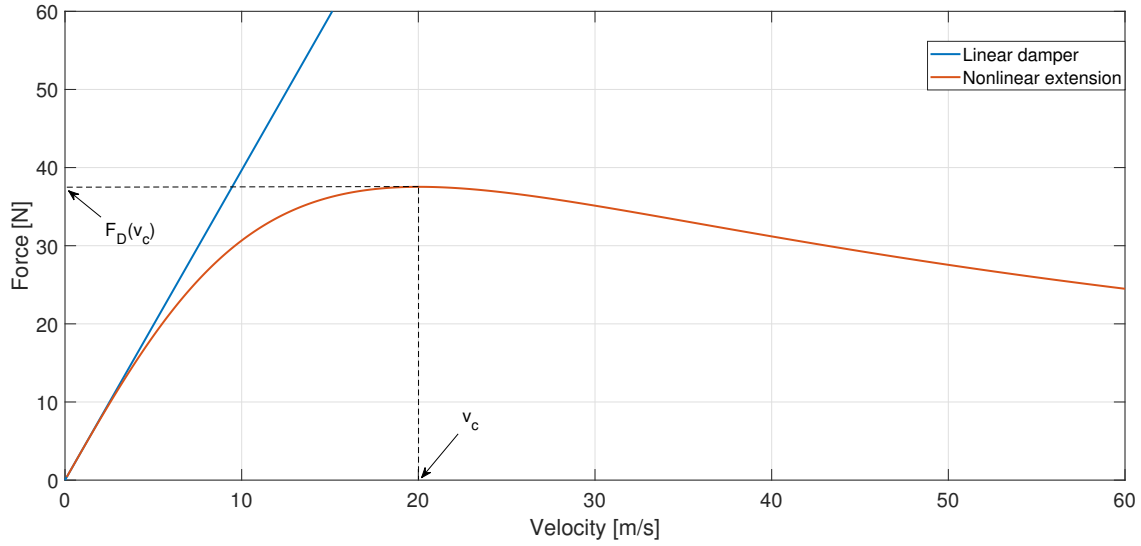

Figure 3.1: Drag force comparison of Wouterse's linear damper and the fitted nonlinear extension for idealized magnetic field $B_0 = 1.0\text{T}$. Critical velocity v_c and corresponding drag force $F_D(v_c)$ are indicated.

The critical velocity at which the maximum drag force is exerted (Figure 3.1) was found to agree with Wouterse's formula (1.12):

$$v_c = w\sqrt{\frac{1}{2}(1+\sqrt{5})} = \frac{2}{\mu_0}\sqrt{(1+\sqrt{5})}\cdot\frac{\nu}{d}\sqrt{\frac{1}{2}} = \frac{2}{\mu_0}\sqrt{\frac{1}{c\xi}}\cdot\frac{\nu}{d}\sqrt{\frac{x}{D}}$$

With compensation factor $c = 1/2$, proportionality factor $\xi = 2/(1+\sqrt{5}) \approx 0.618$ and airgap : pole-diameter ratio $x/D = 1/2$. Since the value of ξ is estimated to be unity, we have an error of $|1-\xi|\cdot 100\% \approx 38.2\%$ which results in a deviation of $|\sqrt{1}-\sqrt{1/\xi}|\cdot 100\% \approx 27.2\%$ in the critical velocity compared to Wouterse's result. Nevertheless, we consider the model sufficiently accurate to warrant further use.

A visual comparison of our fitted nonlinear model (3.4) (Figure 3.1) and experimental results (Figure 1.3) shows a clear improvement in accuracy compared to the linear damper. The dimensions of the experimental results are unclear, but one may claim that our drag force model is roughly proportional to experimental results. We Verify expected proportionality, $F_D \propto v$ for v small and $F_D \propto 1/v$ for v large, by the dominating terms of F_D as

$v \to \{0, \infty\}$:

$$\lim_{v\to 0}\left[\frac{w}{v}\left(1-\frac{w}{(v^2+w^2)^{1/2}}\right)\right] = \lim_{v\to 0}\left(\frac{w(v^2+w^2)^{1/2}-w^2}{v(v^2+w^2)^{1/2}}\right) \sim \left[\frac{0}{0}\right]$$

$$\text{(L'Hôpital's rule)} \to = \lim_{v\to 0}\left(\frac{wv}{2\cdot 2v^2+2w^2}\right) = \lim_{v\to 0}\frac{v}{2w}$$

$$\lim_{v\to\infty}\left[\frac{w}{v}\left(1-\frac{w}{(v^2+w^2)^{1/2}}\right)\right] = \lim_{v\to\infty}\frac{w}{v}$$

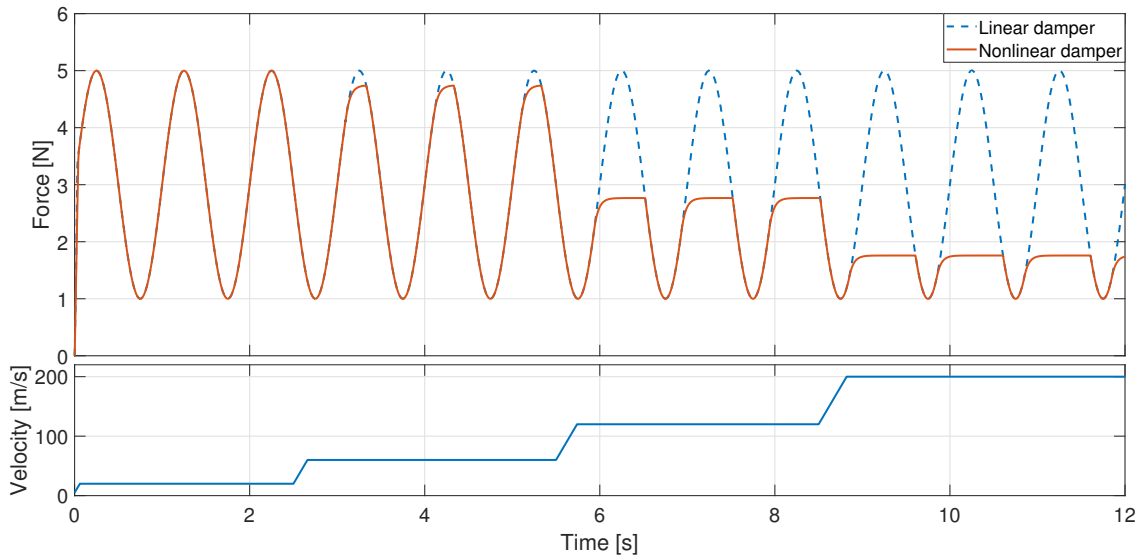

Figure 3.2: Nonlinear model (3.2) performance compared to the idealized model (1.11) for a sinusoidal reference signal $F_r(t)$ and increasing sheet velocity v.

To showcase the limitations of the more realistic nonlinear model, simulations of the drag force models (Figure 3.1) for a smooth $F_r(t)$ were ran side by side (Figure 3.2). The same first order sliding mode control scheme (2.7) was used as in the previous example (Section 2.3). The decay in drag force of the nonlinear model is clearly shown by its saturation for higher speeds. Granted, notable saturation is only present for extremely high velocities in the simulation. For a less modest reference signal however, saturation effects will become significant in a more realistic velocity range. Saturation of F_D for $v >> v_c$ can be avoided by increasing the maximum voltage V_{max} in the SMC, but this requires knowledge of the velocity range of the given application.

3.2 Magnetic Remanence

As seen in the idealized example (Section 2.3), the source voltage required to generate a significant magnetic field using an air core is not attainable in reality. The inductor will instead be winded around a core of some ferromagnetic material (iron, for instance), with drastically higher permeability than air. This will remedy the voltage demand issue, but brings with it another complication in an effect called *magnetic remanence* or *magnetic memory* in the core material.

3.2.1 Problem Description

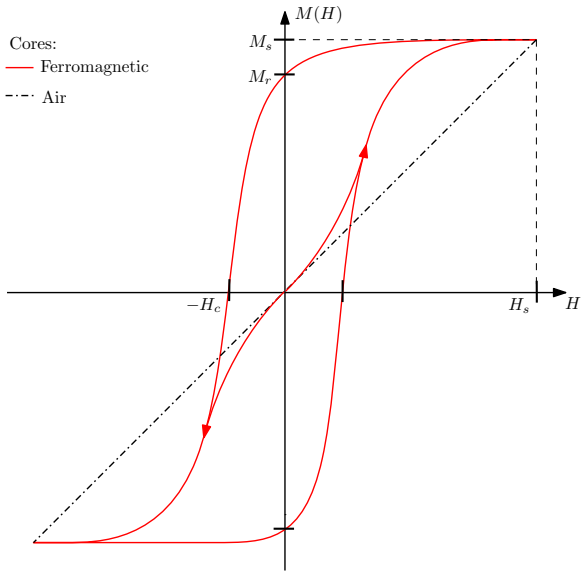

Figure 3.3: Possible magnetic hysteresis loop for an arbitrary ferromagnetic core material, compared with the linear magnetization of an air core.

When an external magnetic field of *magnetic field strength* $\mathbf{H}[\mathrm{A/m}]$ is applied to a ferromagnetic material, the particles in the material become aligned (magnetized) with this field. I.e, the ferromagnetic core gains the *magnetization field* $\mathbf{M}(\mathbf{H})[\mathrm{A/m}]$. We have previously assumed that when the external magnetic field goes away, the particles go back to their original orientation (demagnetized) autonomously. In reality, for large enough H, the material will retain a *remanent magnetization* M_r even as $H \to 0$ (Figure 3.3). For example: The corresponding remanent flux density B_r for a wrought iron core is $B_r = 1.3\mathrm{T}$. This phenomenon is the basis for the creation of permanent magnets, but is generally unwanted

behaviour in electromagnets as demagnetization of the core requires excitation of an oppositely directed magnetic field. The magnetic field strength required to fully demagnetize the core, is called the *coercivity* H_c of the material.
On top of increased complexity in the ECB actuator, unwanted effects of magnetic hysteresis includes energy losses [19, ch. 2]. Energy is lost due to the cycling between remanence and coercivity (Figure 3.3), and in the form of heat due to the induction of eddy currents within the core.
Previously we have assumed a linear relation between *flux density* **B** and **H**: $B = \mu H$. In general, $B(H)$ shares the nonlinear behaviour of $M(H)$ for non-air cores: $B(H) = \mu M(H)$ in core material of permeability μ.

3.2.2 Mathematical Models

Most mathematical representations of the phenomenon are in the form of nonlinear hysteresis models. The Preisach-Krasnoselskij approach is a mathematical generalization by Krasnoselskij [20] of the widely accepted discrete scalar model of magnetic hysteresis proposed by Preisach [21]. Preisach's proposed model is a decomposition of the hysteresis curve into an infinite sum of relay switching functions $\hat{\gamma}_{\alpha_i,\beta_i}$, where the (α_i, β_i) pairs denote the switching thresholds (lower and upper, respectively). The relay functions each represent a magnetic dipole. Krasnoselskij's generalized formulation of systems with hysteresis states:

$$f(t) = \iint_{\alpha \geq \beta} \mu(\alpha, \beta)\hat{\gamma}_{\alpha,\beta}(u(t))d\alpha d\beta \tag{3.5}$$

Where $(u(t), f(t))$ is an arbitrary input-output pair, and $\mu(\alpha, \beta)$ is an arbitrary weighting function. The curve $B(H)$ can be expressed as:

$$B = \iint_{S} \mu(\alpha, \beta)\hat{\gamma}_{\alpha,\beta}(H)d\alpha d\beta \tag{3.6}$$

In the triangular region S: $H_{sat} \geq \alpha \geq \beta \geq -H_{sat}$, where the dipoles are distributed according to $\mu(\alpha, \beta)$.

3.2.3 Relevant Literature

In [22], the following approximation of the nonlinear B/H curve (Figure 3.3) was shown to be sufficiently accurate in ECB applications:

$$B(H) = \begin{cases} B_r + \mu H \text{ for } H > 0 \\ [B_r, -B_r] \text{ for } H = 0 \\ -B_r + \mu H \text{ for } H < 0 \end{cases} \tag{3.7}$$

Where μ is the permeability of the given material and the magnetic field excited by a current i through N inductor windings around a core of length l is given by $H = Ni/l$. In [10], (3.7) was used to extend the linear brake force model (1.11):

$$f_b = (\alpha_0 + \alpha_1 i_{cmd} + \alpha_2 i_{cmd}^2)v \tag{3.8}$$

The model parameters α_i are:

$$\begin{aligned} \alpha_0 &= f_0 + \frac{\pi}{4\nu} D^2 d B_r^2 c \\ \alpha_1 &= \pm \frac{\pi}{2\nu} D^2 d B_r c \frac{N}{l} \mu \\ \alpha_2 &= \frac{\pi}{4\nu} D^2 d c \left(\frac{N}{l} \mu \right)^2 \end{aligned}$$

Where f_0 is the natural friction coefficient of the process, and c is given by (1.10). The model was used in a feedback-linearization control scheme of the angular velocity of a conductive disk with variable driving torque. Parameter estimation prior to each experiment, as well as real time output estimation using an observer, was used to yield a seemingly robust method. Experimental results showed good performance in the low speed region, but high speed region performance was not investigated as the model does not account for the corresponding demagnetizing effects (Section 3.1).

To the author's knowledge, There are no models in the available literature on ECBs accounting for both the demagnetizing effects of high speeds and magnetic hysteresis in the electromagnet. Assuming high speed demagnetization and magnetic hysteresis are isolated effects, one might consider extending the high speed model (3.4) to account for hysteresis

effects as well. The proposed model is given by:

$$
\begin{aligned}
F_D &= \frac{\pi c D^2}{\mu_0}\frac{w}{v}\left(1 - \frac{w}{(v^2+w^2)^{1/2}}\right)B(H)^2 \\
B(H) &= \begin{cases} B_r + \mu_0 H & \text{for } H > 0 \\ [B_r, -B_r] & \text{for } H = 0 \\ -B_r + \mu_0 H & \text{for } H < 0 \end{cases} \\
H &= \frac{Ni}{l_g}
\end{aligned}
\tag{3.9}
$$

As stated, the above model makes no appearance in the publications included in the ECB literature review. Thus, the accuracy of the model is unclear with the lack of experimental results.

3.3 More Control Algorithms

3.3.1 Optimal Linear Control

The performance loss of the ECB for high velocities may put high requirements for the maximum voltage of the controller to avoid saturation of F_D. If we are to continue using a SMC, this may lead to complications in the physical implementation. Specifically, researchers who have implemented SMC on magnetic braking systems have cited issues regarding heat generation in the electromagnetic current, in some cases damaging the components. This motivates the use of a Linear Quadratic Regulator (LQR) to replace the SMC, such that we can weight the system dynamics accordingly to avoid damaging the actuator.

To achieve continuous optimal control, a feedback controller $\mathbf{u}(t) = -\mathbf{K}(t)\mathbf{x}(t)$ is chosen such that the infinite horizon cost function

$$J = \frac{1}{2}\int_{t_0}^{\infty} \Big(\mathbf{x}(t)^T \mathbf{Q}(t)\mathbf{x}(t) + \mathbf{u}(t)^T \mathbf{R}(t)\mathbf{u}(t) \Big) dt \tag{3.10}$$

is minimized. In (3.10), $\mathbf{Q}(t) \in \Re^{n\times n}$ and $\mathbf{R}(t) \in \Re^{m\times m}$ are weighting matrices on the state vector $\mathbf{x}(t) \in \Re^n$ and input vector $\mathbf{u}(t) \in \Re^m$ respectively. Additionally, the weighting matrices are positive definite: $\mathbf{Q}(\cdot), \mathbf{R}(\cdot) > 0$ and their entries are design parameters. Traditional LQR implementations [23] assume a linear plant

$$\dot{\mathbf{x}}(t) = \mathbf{F}\mathbf{x}(t) + \mathbf{G}\mathbf{u}(t) \tag{3.11}$$

which means we want to express our system dynamics in accordance with (3.11) for ease of implementation and ensured stability and optimality conditions. Since the underlying dynamics of the electromagnet circuit are linear and the nonlinearity is limited to the output, we may consider linear control methods. $\mathbf{K}(t)$ is given by:

$$\begin{aligned} \mathbf{K}(t) &= \mathbf{R}^{-1}(t)\mathbf{G}^T(t)\mathbf{P}(t), \quad \mathbf{P}(\cdot) > 0 \\ -\dot{\mathbf{P}}(t) &= \mathbf{P}(t)\mathbf{F}(t) + \mathbf{F}^T(t)\mathbf{P}(t) - \mathbf{P}(t)\mathbf{G}(t)\mathbf{R}^{-1}(t)\mathbf{G}(t)^T\mathbf{P}(t) + \mathbf{Q}(t) \end{aligned}$$

If we consider the sheet velocity $v(t)$ a slowly varying measurable external disturbance, and we can say that $\dot{v}(t) \approx 0$ for any given t, we get the following quasi-static model for

nonlinear drag force dynamics:

$$\begin{aligned}
\frac{d}{dt}i(t) = \dot{x}_1 =& -\frac{R_{mag}}{L}x + \frac{1}{L}u \\
\dot{F}_D(t) = \dot{x}_2 =& \, 2 \cdot \frac{\pi c D^2}{\mu_0}\frac{w}{v}\left(1 - \frac{w}{(v^2+w^2)^{1/2}}\right)B_0\dot{B}_0 \\
=& -2\pi c D^2 \frac{w}{v}\left(1 - \frac{w}{(v^2+w^2)^{1/2}}\right)\frac{\mu_0 N^2 R_{mag}}{l_g^2 L}x_1^2 \\
&+ 2\pi c D^2 \frac{w}{v}\left(1 - \frac{w}{(v^2+w^2)^{1/2}}\right)\frac{\mu_0 N^2}{l_g^2 L}x_1 u \\
=& -2\frac{R_{mag}}{L}x_2 + 2\frac{1}{L}\frac{x_2}{x_1}u
\end{aligned} \tag{3.12}$$

Where B_0 is given by (2.6). Due to the proportionality $F_D \propto B_0^2 \propto i^2$, this is not a linear model (3.11). Linear feedback control methods such as LQR can in some cases be applied directly to nonlinear systems, but useful properties such as preserved passivity do not hold in general - due to the superposition principle not applying to nonlinear systems. In our case (3.12) it can be shown that the system has an asymptotically stable origin for a state feedback input $u = -kx$ and output $y = F_D = C_D x^2$, while the same cannot be said for the output feedback input $u - ky$.

$$\begin{aligned}
V(y) =& \frac{1}{2}y^2 \\
\dot{V}(y) =& y\dot{y} = C_D x^2(-2C_D\frac{R_{mag}}{L}x^2 + 2\frac{1}{L}xu) \\
=& -2C_D^2\frac{R_{mag}}{L}x^4 + 2\frac{1}{L}x^3 u \\
\leq& -\frac{2C_D^2}{L}kx^4 < 0\,, \;\forall x \in \Re/\{0\}
\end{aligned}$$

In order to ensure trajectory tracking $\tilde{y} = y_r - y$, we may instead express this behaviour in terms of the state variable. This is preferable, as input-output stability is guaranteed for state feedback inputs. If we instead define the manipulated variable as $\sqrt{F_D}$, we can identify the quasi-static linear model:

$$\begin{aligned}
\frac{d}{dt}\left(\sqrt{F_D}\right) =& \left[\frac{\pi c D^2}{\mu_0}\frac{w}{v}\left(1 - \frac{w}{(v^2+w^2)^{1/2}}\right)\right]^{1/2}\frac{d}{dt}|B_0(t)| \\
=& -\left[\pi c D^2 \mu_0 \frac{w}{v}\left(1 - \frac{w}{(v^2+w^2)^{1/2}}\right)\right]^{1/2}\frac{N R_{mag}}{l_g L}|i(t)| \\
&+ \left[\pi c D^2 \mu_0 \frac{w}{v}\left(1 - \frac{w}{(v^2+w^2)^{1/2}}\right)\right]^{1/2}\frac{N}{l_g L}\text{sgn}(i(t))V_{cmd}(t)
\end{aligned} \tag{3.13}$$

The model (3.13) is valid as long as $F_D \geq 0$ such that $\sqrt{F_D} \in \Re$, which is satisfied by $v = |\mathbf{v}| \geq 0$. We choose to constrict the current to positive values, so that $\big(|i(t)|, \text{sgn}(i(t))V_{cmd}(t)\big) = \big(i(t), V_{cmd}(t)\big)$ and (3.13) satisfies (3.11). We make the observation that if the sheet speed is assumed constant at time t, the linear system (3.13) is simply a linear combination of the circuit dynamics (2.2). Thus, we need only consider the scalar case with $i(t)$ as the only state variable.
Noting that $\tilde{y} = \sqrt{F_{D_r}} - \sqrt{F_D} \to 0 \Rightarrow F_D \to F_{D_r}$ for $\{F_D, F_{D_r}\} \geq 0$, a possible cost function is of the form:

$$\begin{aligned} J &= \frac{1}{2}\int_{t_0}^{\infty} \Big(\rho\big[\sqrt{F_{D_r}} - \sqrt{F_D}\big]^2 + rV_{cmd}^2\Big)dt \\ &= \frac{1}{2}\int_{t_0}^{\infty} \Big(C_D\rho\big[i_r - i\big]^2 + rV_{cmd}^2\Big)dt \end{aligned} \tag{3.14}$$

The above conditions correspond to a constrained quadratic optimization problem,

$$\min_u J(i, i_r, u) = \min_u \frac{1}{2}\int_{t_0}^{\infty} \Big(\rho'\big[i_r - i\big]^2 + ru^2\Big)dt$$

subject to:

$$\begin{aligned} &\{i, i_r\} \geq 0\ , \\ &|u| \leq V_{max} \end{aligned} \tag{3.15}$$

the analytic solution of which is given by the Hamilton-Jacobi equation [23, ch. 2.2] with J as the performance index:

$$\frac{\partial J^*}{\partial t} = -\min_u \left\{\rho'(i_r - i)^2 + ru^2 + \frac{\partial J^*}{\partial(i_r - i)}\frac{d}{dt}(i_r - i)\right\} \tag{3.16}$$

Inserting $u = -k(i_r - i) = -k\tilde{i}$ into (3.16), we get the optimal feedback control law:

$$\begin{aligned} u^* = -k^*\tilde{i} &= -\arg\min_k \left\{\rho'\tilde{i} + k^2 r\tilde{i}^2 + \frac{\partial}{\partial\tilde{i}}(\rho'\tilde{i}^2 + k^2 r\tilde{i})\dot{\tilde{i}}\right\}\tilde{i} \\ &= -\arg\min_k \left\{\rho'\tilde{i}^2 + k^2 r\tilde{i}^2 + 2\rho'\tilde{i}(-\frac{R_{mag}}{L} - \frac{1}{L}k)\tilde{i}\right\}\tilde{i} \\ &= -\arg\min_k \left\{(k^2 r - 2\frac{1}{L}\rho' k + \rho' - 2\frac{R_{mag}}{L}\rho')\tilde{i}\right\}\tilde{i} \\ &= -\frac{1}{Lr}\rho'\tilde{i} \end{aligned} \tag{3.17}$$

The heat generated in the electromagnetic circuit can be modelled simply as:

$$P_{mag}(t) = R_{mag}i(t)^2 \tag{3.18}$$

Where $P_{mag}(t)$ is the electric power of the electromagnetic circuit at time t. This is a quadratic term that we may include in the cost function (3.10) if we want to penalize overheating due to high currents.

3.3.2 Higher Order SMC With Equivalent Control

To compare with the performance of our LQR design, some improvements on the SMC used in the first example (Section 2.3) were implemented. The original controller used in the example actually corresponds to a zero order SMC, where the sliding mode is given by $s = y - y_r$, but has no action to make sure the system *stays* there. Instead of using continuous approximations of the Heaviside function as the only method to prevent chattering, other methods not accompanied by stationary deviations were explored. In particular, higher order sliding mode and equivalent control were considered as alternatives. As previously mentioned, these methods have been used to great effect in ECB ABS applications [7, 8].

Consider the scalar, nonlinear, time-varying system:

$$\begin{aligned} x &= f(x, u, t) \\ y &= h(x, u, t) \\ \tilde{y} &= y - y_r \end{aligned} \tag{3.19}$$

Where $y_r$is the desired output, and $\tilde{y}$ is the tracking error. In (3.19), let $u(t)$ be given by Slotine and Li's definition of SMC [24, ch. 7]. In the cited publication, the sliding surface $s = 0$ corresponding to desired behaviour of the system is generally given by the expression:

$$s = \left(\frac{d}{dt} + \lambda \right)^{(n-1)} \tilde{y} \tag{3.20}$$

Where $n > 0$ is the order of the sliding mode, and $\lambda > 0$ is a design parameter typically selected based on the frequency range of unmodeled dynamics. Observe, for instance, how $\lambda > 0$ ensures asymptotically stable tracking error at $\tilde{y} = 0$ on a second order ($n = 2$) sliding surface: $s = 0 \Rightarrow \dot{\tilde{y}} = -\lambda \tilde{y}$.
Continuous *Equivalent Control* u_{eq} is given by explicit solution of the sliding dynamics $\dot{s} = 0$. u_{eq} then corresponds to the control law that would, if the dynamics of the system were exactly known, *keep the system on* the sliding surface: $s = \dot{s} = 0$. If the system is uncertain, the discontinuous *Reaching Control* component $u_r = -k \cdot \text{sgn}(s)$ is necessary to fulfill the reachability condition (2.1) - and to *guide the system to* the sliding surface. Adding the equivalent and reaching control components, yields the sliding mode control

law:

$$u = u_{eq} + u_r \tag{3.21}$$

In most cases, smooth approximation of the discontinuous reaching control is desirable. For this purpose, we use a saturation function interpolating the values of s within a thin boundary layer $\psi > 0$:

$$\text{sat}\left(\frac{s}{\psi}\right) = \begin{cases} \frac{s}{\psi} & , \ \frac{|s|}{\psi} < 1 \\ \text{sgn}(\frac{s}{\psi}) & , \ \text{otherwise} \end{cases} \tag{3.22}$$

Application of the control law (3.21) to our first-order braking force system,

$$\begin{aligned} \dot{x} &= \frac{d}{dt}i(t) = -\frac{R_{mag}}{L}i(t) + \frac{1}{L}V_{cmd}(t) \\ y &= F_D = \pi c D^2 \frac{w}{v}\left(1 - \frac{w}{(v^2+w^2)^{1/2}}\right)\frac{\mu_0 N^2}{l_g^2}i(t)^2 = C_D i(t)^2 \\ V_{cmd} &= u_{eq} + u_r \end{aligned} \tag{3.23}$$

for a conductive sheet of infinite length, requires a few modifications to both the sat()-function and the control law due to the lack of a driving force. First, we choose u_r and u_{eq} in accordance with [24, 25, ch. 7, ch. 14.1]:

$$\begin{aligned} u_r(i,s,t) &= -\eta(i)\text{sat}(\frac{s}{\psi}) \\ \dot{s} &= \dot{F}_D - 0 = -2C_D\frac{R_{mag}}{L}i(t)^2 + 2C_D\frac{1}{L}i(t)u_{eq} = 0 \\ \Rightarrow u_{eq}(i,t) &= R_{mag}i(t) \end{aligned}$$

Assume that $\{F_D, F_{D_r}\} \geq 0$, and that the desired braking force is constant: $F_{D_r}(t) = F_{D_r}$. Define the first order sliding surface as: $s = \tilde{F}_D = F_D - F_{D_r}$, and let a proposed control law for the command voltage be given by:

$$\begin{aligned} V_{cmd}(i,s,t) &= u_r(i,s,t) + u_{eq}(i,s,t) = \begin{cases} u_r(i,s,t) + u_{eq}(i,t) & \text{for } \frac{s}{\psi} < 1 \\ 0 & \text{otherwise} \end{cases} \\ u_r(i,s,t) &= -\eta(i)\text{sat}(\frac{s}{\psi}) = \begin{cases} -\eta(i)\frac{s}{\psi} & \text{for } \frac{|s|}{\psi} < 1 \\ -\eta(i)\text{sgn}(s) & \text{for } \frac{s}{\psi} \leq -1 \\ 0 & \text{for } \frac{s}{\psi} \geq 1 \end{cases} \\ u_{eq}(i,t) &= R_{mag}i(t) \end{aligned} \tag{3.24}$$

Reachability verification (2.1) of the sliding surface $s = 0$ by Lyapunov analysis for the Lyapunov candidate function $V(s) = \frac{1}{2}s^2$:

$$\dot{V}(s) = s\dot{s} = s\dot{F}_D = -2C_D\frac{R_{mag}}{L}i(t)^2 s + 2C_D\frac{1}{L}i(t)sV_{cmd}(i,s,t)$$

$\underline{|s|/\psi \geq 1\text{:}}$

$$\begin{aligned}
s<0:\ \dot{V}(s) &= -2C_D\frac{R_{mag}}{L}i(t)^2 s - 2C_D\frac{1}{L}i(t)s\eta(i)\text{sgn}(s) + 2C_D\frac{R_{mag}}{L}i(t)^2 s \\
&= -2(1-s)C_D\frac{R_{mag}}{L}i(t)^2 - 2C_D\frac{1}{L}\eta(i)|s| \leq -2C_D\frac{1}{L}i(t)\eta(i)|s| \\
&\leq -k|s|,\ k>0 \text{ for } \eta(i) = \frac{L}{2C_D i(t)}\cdot k,\ i(t)\neq 0 \\
&\rightarrow \underline{\text{boundary layer is reachable "from below" } (s \leq -\psi)}
\end{aligned}$$

$$\begin{aligned}
s>0:\ \dot{V}(s) &= -2C_D\frac{R_{mag}}{L}i(t)^2 s + s\cdot 0 \\
&(s>0 \Rightarrow F_D > F_r \geq 0 \Rightarrow i(t)\neq 0) \\
&= -2C_D\frac{R_{mag}}{L}i(t)^2 s < 0,\ \forall s>0 \\
&\rightarrow \underline{\text{system reaches boundary layer in finite time "from above" } (s \geq \psi)}
\end{aligned}$$

$\underline{|s|/\psi < 1\text{:}}$

$$\begin{aligned}
\dot{V}(s) &= -2C_D\frac{R_{mag}}{L}i(t)^2 s + 2C_D\frac{1}{L}i(t)s[(-\frac{Lk}{2C_D i(t)}\cdot\frac{s}{\psi} + R_{mag}i(t)] \\
&= -2C_D\frac{R_{mag}}{L}i(t)^2 s - k\frac{s^2}{\psi} + 2C_D\frac{R_{mag}}{L}i(t)^2 s \\
&= -k\frac{s^2}{\psi} = -k\frac{|s|^2}{\psi} < -k|s|,\ \forall s\in(-\psi,\psi) \\
&\rightarrow \underline{s=0 \text{ is reachable from within the boundary layer}}
\end{aligned}$$

This result proves that convergence to $s = 0$ in finite time is guaranteed for constant reference signals, assuming the *convergence rate* k is chosen large enough to counteract any uncertainties in the system parameters.

A more traditional first order SMC design can be found by defining the sliding surface in the same manner is in the section on LQR design (Section 3.3.1):

$$\begin{aligned}
s = \tilde{y} &= \sqrt{F_D(t)} - \sqrt{F_{D_r}} \\
&= \sqrt{C_D i(t)^2} - \sqrt{C_D i_r^2} = \sqrt{C_D}\big(|i(t)| - |i_r|\big)
\end{aligned} \tag{3.25}$$

Reachability conditions are fulfilled by choosing $u = u_r + u_{eq}$ such that $\dot{s} = -k\text{sat}\big(\frac{s}{\psi}\big)$, $k > 0$:

$$\begin{aligned} \dot{s} &= -\frac{R_{mag}}{L}\sqrt{C_D}|i(t)| + \frac{1}{L}\sqrt{C_D}\text{sgn}\big(i(t)\big)u(t) = -k\text{sat}\left(\frac{s}{\psi}\right) \\ \Rightarrow u(t) &= -\frac{L}{\sqrt{C_D}\text{sgn}\big(i(t)\big)}k\text{sat}\left(\frac{s}{\psi}\right) + R_{mag}i(t) \\ &= u_r(t) + u_{eq}(t) \end{aligned} \tag{3.26}$$

Chapter 4

Results and Discussion

Results of the literature survey and implementation of the methods described in (Chapter 3) will be presented and discussed in this chapter. Simulation results are based on the framework described in (Section 2.3).

4.1 Linear Optimal Control

This section contains the simulation results of the optimal linear feedback controller derived in (Section 3.3.1). Dynamic model and control law expressions were implemented in a MATLAB script, using the explicit midpoint rule with step-size $h = 10^{-7}$ as the simulation method:

$$y_{n+1} = y_n + hf\left(t_n + \frac{h}{2}, y_n + \frac{h}{2}f(t_n, y_n)\right) \tag{4.1}$$

Which was chosen due to stability issues using simple Euler integration. The maximum voltage (3.15) was chosen equal to the common voltage of Norwegian electrical outlets: $V_{max} = 230\text{V}$. It is assumed that the force sensor measurement (Figure 2.3) is instantaneous: $y(t) = F_D(t)$.

By tuning the LQR parameters to heavily weight the tracking error (Figure 4.1), the model

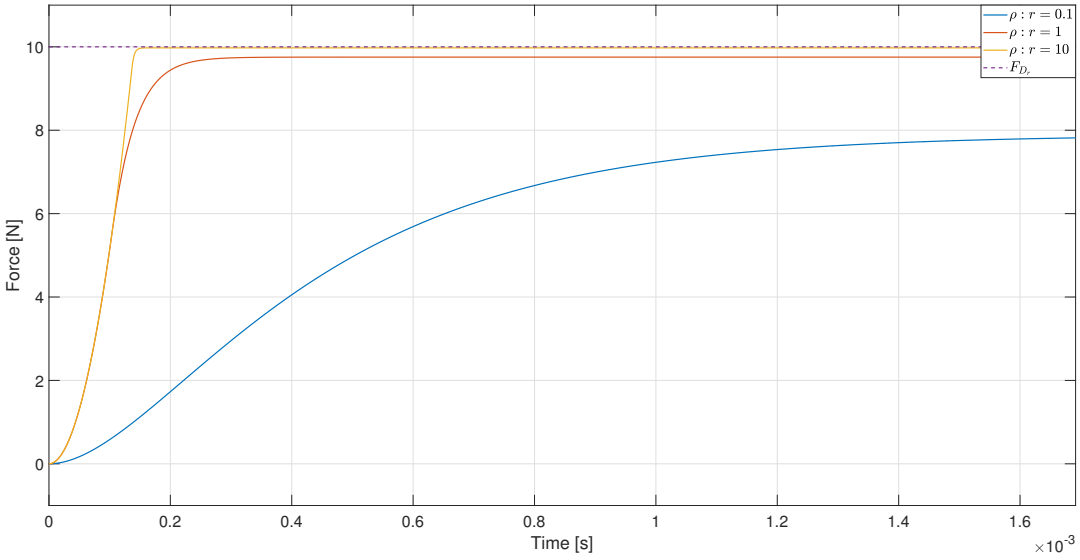

Figure 4.1: Tuning of the error/input penalization parameters ρ, r.

(3.4) converges to a constant reference braking force for a constant sheet speed $v(t) = v_0 = 5\text{m/s}$. Furthermore, the controller successfully tracks a time-varying reference well into the high speed region with only minor command voltage saturation (Figure 4.2 and 4.3).

Judging by the tracking performance when the uncertainties due to demagnetization in the

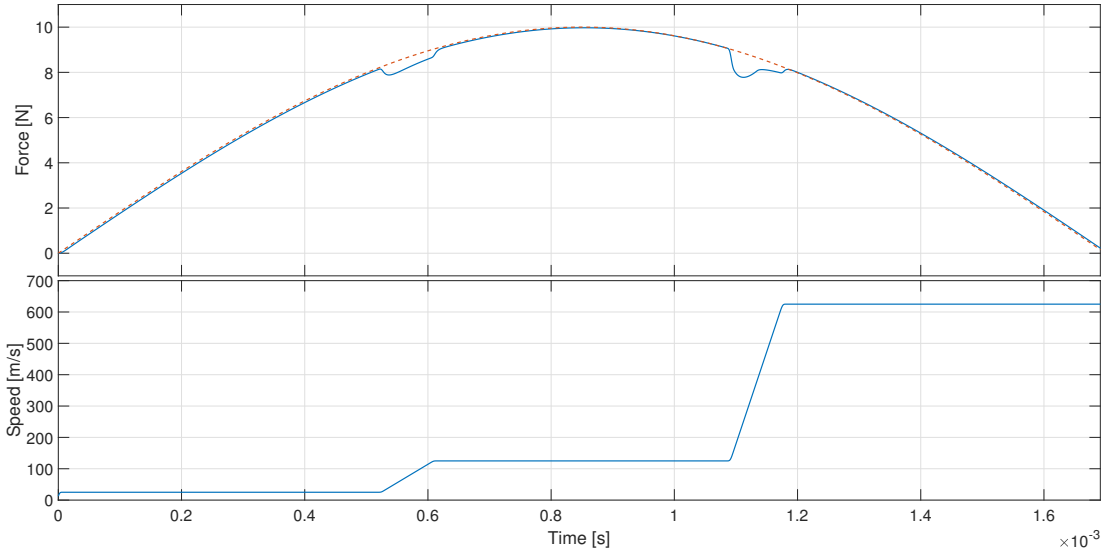

Figure 4.2: High speed brake force tracking of time-varying reference of the tuned LQR.

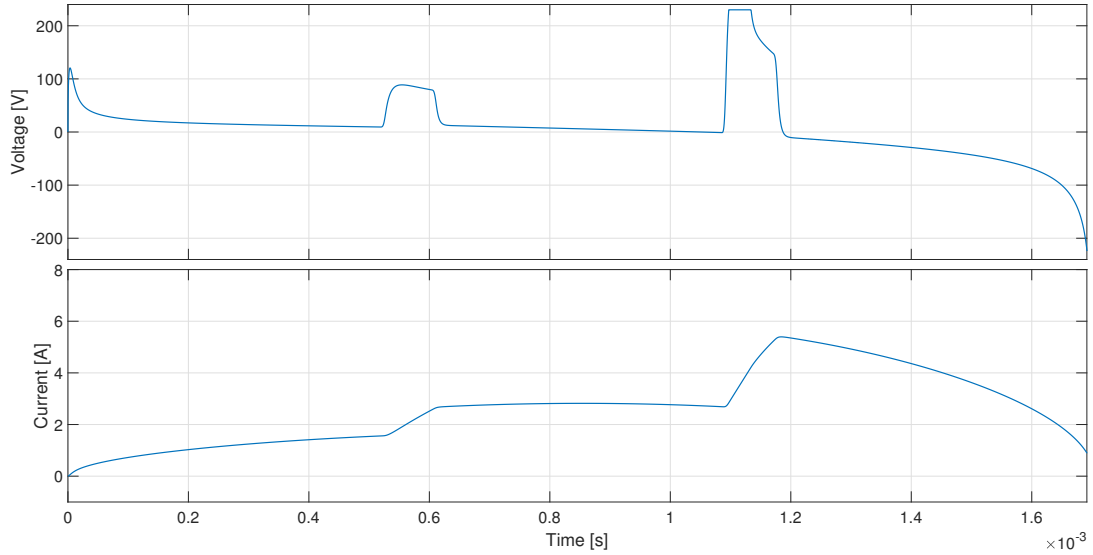

Figure 4.3: Optimal control time-series corresponding to (Figure 4.2).

high speed region (Figure 4.4) are unmodeled, robustness of the stationary LQR is lacking. Convergence to a constant reference can however be achieved with higher weighting of the tracking error (Figure 4.5 and 4.6). The LQR is thus "robust" in the sense that it can be tuned to give convergence despite parameter uncertainties on a priori basis, but the

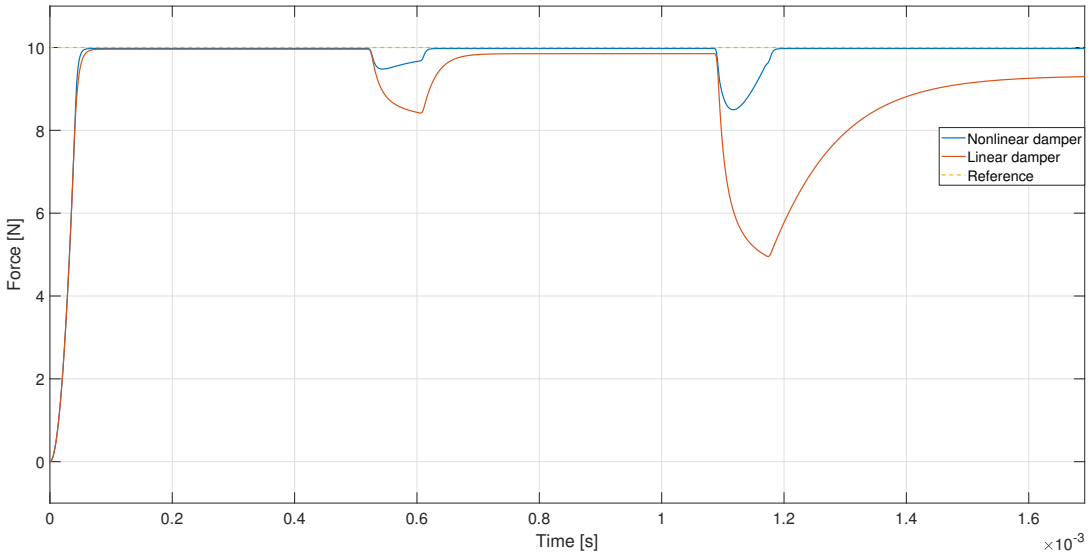

Figure 4.4: System output responses of the LQR, where the demagnetizing effects of the sheet velocity (Figure 4.2) are modeled (blue) or unmodeled (red) - assuming that the nonlinear damper (3.4) models the plant perfectly.

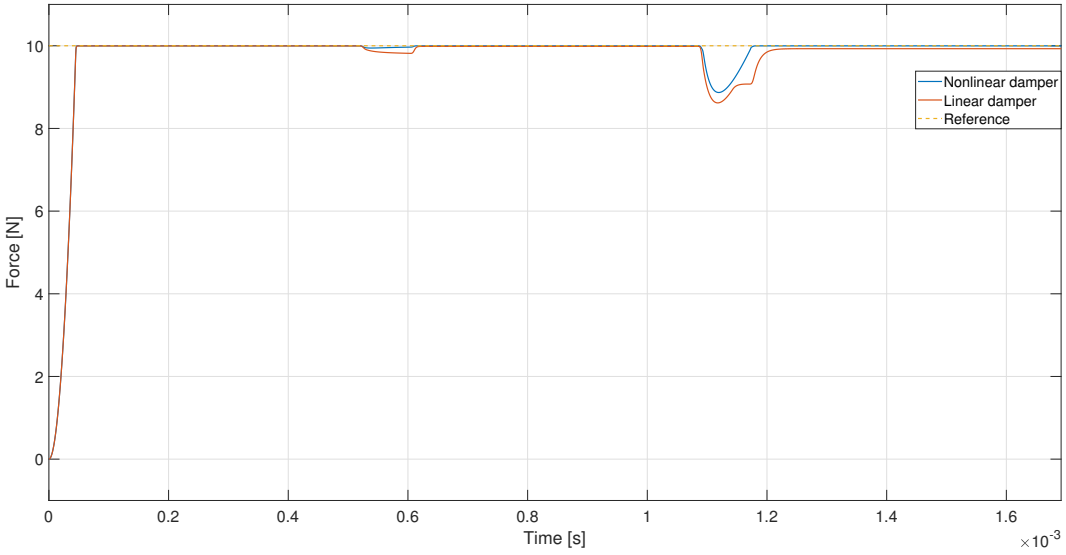

Figure 4.5: Same scenario as in (Figure 4.4) where the LQR has been tuned such that $\rho : r = 100$, leading to improved tracking.

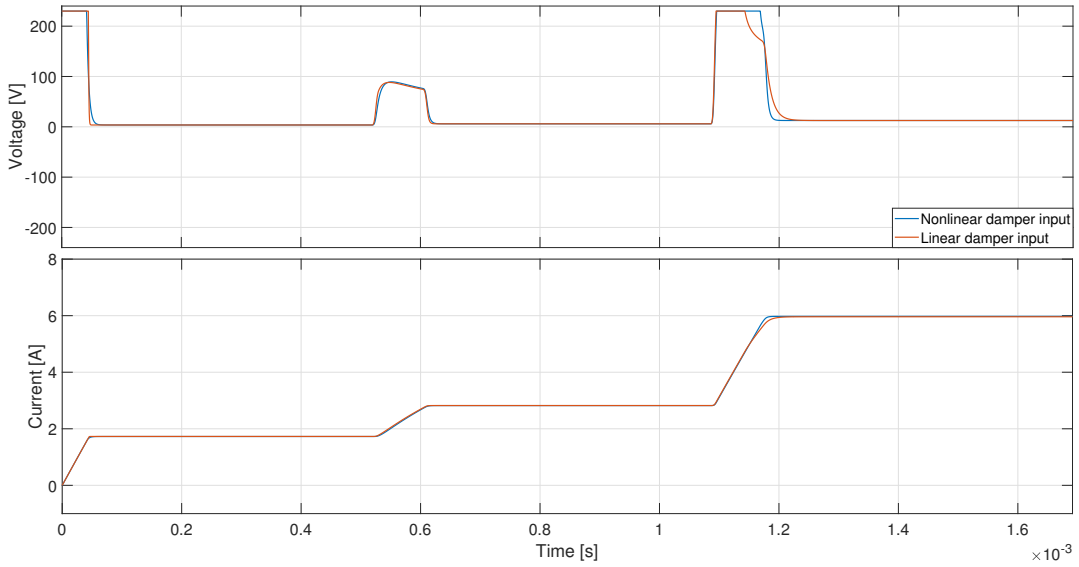

Figure 4.6: Command voltage and current time-series comparison for linear and nonlinear dampers (Figure 4.5).

stationary LQR in this form lacks the adaptivity we are looking for in an application where the analytical model is very uncertain. Ensuring convergence by letting $\rho/r \to \infty$ is not preferred, as it results in the exact same drawbacks as in the first SMC implementation (Section 2.3).

Another limitation of the controller is the presence of unmodeled dynamics, such as in the force sensor. To increase robustness of the LQR to both unmodeled dynamics and parameter uncertainties, one might consider adding a dimension to the control system in the form of an integral state augmentation. Of course, this introduces its own drawbacks, such as integral windup due to command voltage saturation, and a significantly increased time-constant of the system response.

4.2 SMC With Equivalent Control

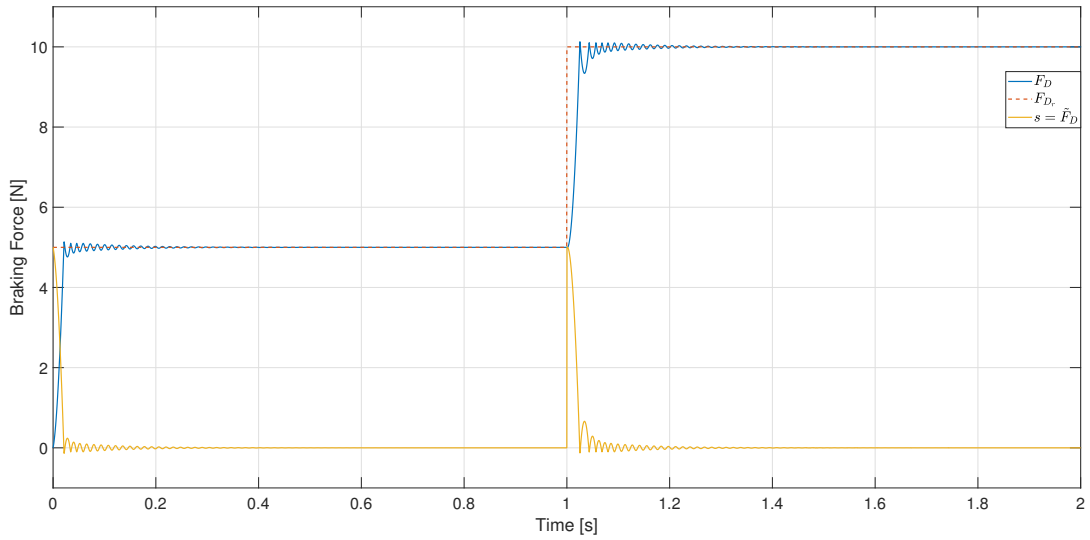

Figure 4.7: First order SMC trajectory tracking with boundary layer $\psi = 0.1$ and convergence rate $k = 1000$.

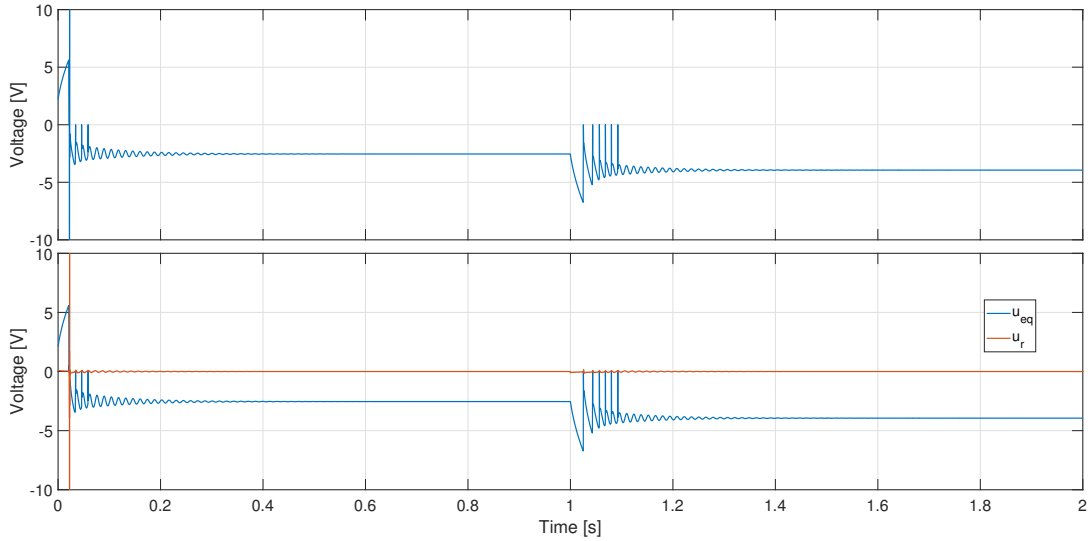

Figure 4.8: Top: Command voltage from the SMC, yielding the trajectory (Figure 4.7). Bottom: Reaching and equivalent control components of the command voltage.

First order SMC designs with equivalent control, as described in (Section 3.3.2), were implemented on the brake force model (3.4) and tested for various values of sheet speed and brake force trajectories. Design parameters ψ and k were chosen by trial and error.

This time, the inertia of an arbitrary force sensor was included and implemented as a simple first order differential equation:

$$\tau_d \dot{y} = -y + F_D$$
$$\frac{y}{F_D}(s) = \frac{1}{\tau_d s + 1} = \frac{1}{0.05s + 1}$$

Where τ_d is as an approximation of the *Charge-/Discharge Time Constant* (CTC, DTC) property of piezoelectric force sensors. The sensor dynamics will remain unmodeled from the perspective of the controller, and will serve to demonstrate the strengths and weaknesses of the SMC in the presence of unmodeled dynamics. The ECB model with both SMCs were implemented individually and simulated using MATLAB & Simulink.

From initial results of the modified (3.24) SMC (Figure 4.7 and 4.8) we observe that the braking force converges to a constant reference signal, but is subject to oscillations caused by the unmodeled sensor dynamics. In particular, observe how the reaching controller component remains very small despite the oscillations reaching far outside of the boundary layer. We can also observe discontinuities in both reaching and equivalent control components, due to the modification of the algorithm.

The negative effects of a disturbance in the system in the form of *Gaussian White Noise* (GWN) (Figure 4.9) large enough to push the system outside of the boundary layer can be partly mitigated by increasing the convergence rate k and/or reducing the boundary layer ψ (Figure 4.10 and 4.11). By doing this, we may force the system as close to the sliding surface as we want despite the stochastic disturbance - the adverse effects of this is obvious from the command voltage time-series: Since both components of our modified SMC are discontinuous, we get high frequency switching in the command voltage - made worse by the choice of ψ. Another interesting observation is that the reaching control component (voltage spikes outside of the scope) is activated when the system is pushed outside of the boundary layer due to the disturbance, which was not the case for deviations caused by unmodeled sensor dynamics.

If we consider instead the traditional SMC design (3.26) with *continuous* equivalent control, we can see the impact of the unmodeled dynamics more clearly (Figure 4.13). While the system converges to the sliding surface despite unmodeled dynamics, they are clearly detrimental to the controller performance. In particular, the SMC overshoots the sliding surface by a large margin. This overshoot in braking force output of course corresponds

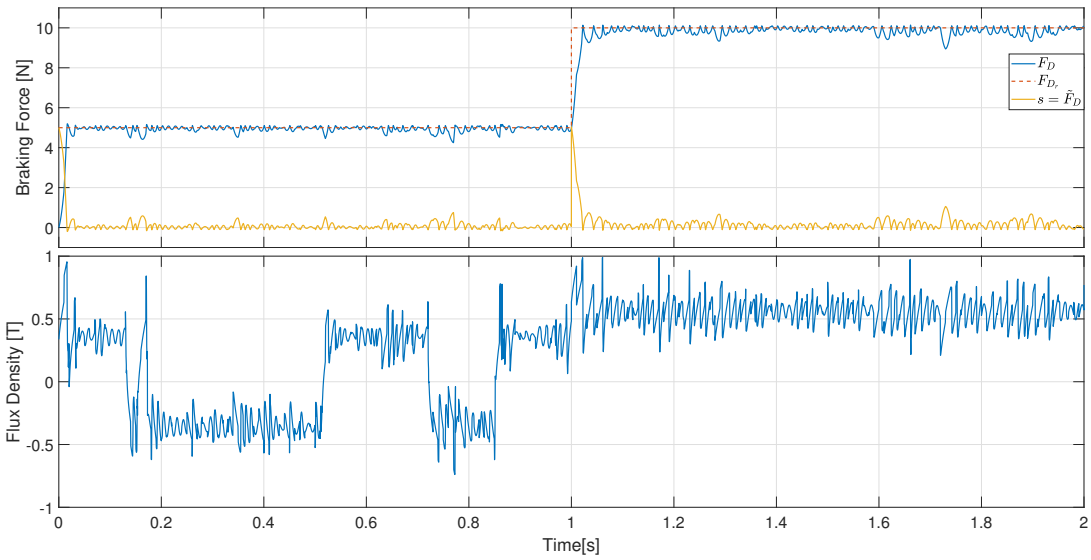

Figure 4.9: Tracking performance of SMC with stochastic flux density. $\psi = 0.1$, $k = 1000$.

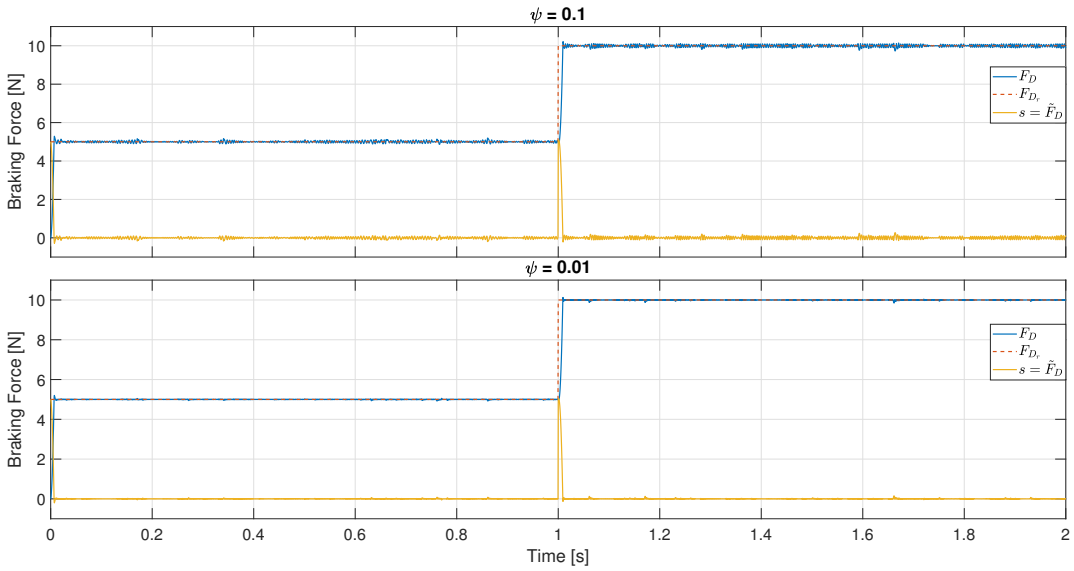

Figure 4.10: Tracking performances of SMC on model with disturbance for reduced boundary layer thickness ψ. $k = 10000$.

to a larger than necessary current in the circuit, that will shorten the lifespan of components unnecessarily. The overshoot can be reduced by reducing k, but this is undesirable as controller efficiency and robustness will be reduced as well. Changing ψ has no effect,

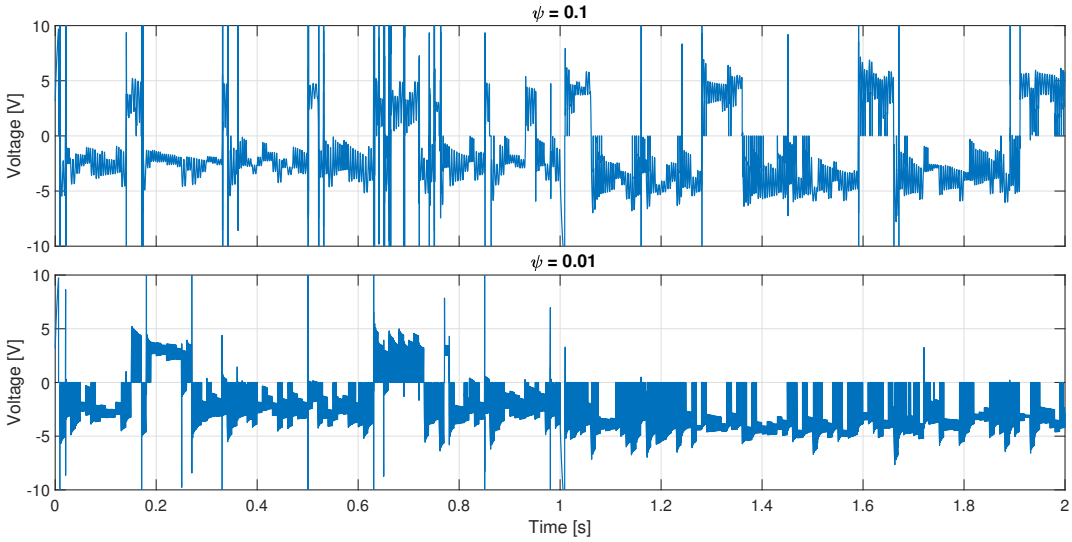

Figure 4.11: SMC command voltages behind the above trajectories. (Figure 4.10).

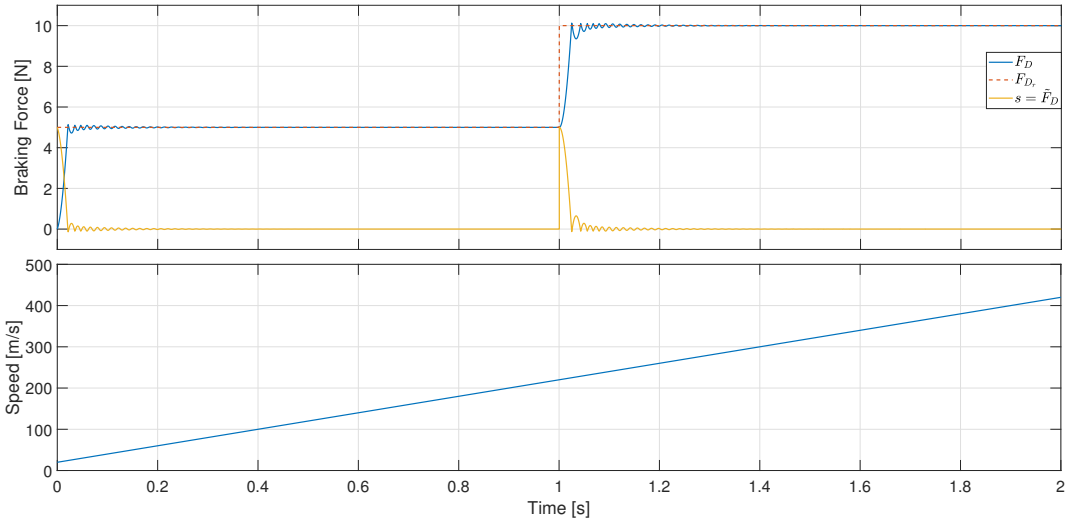

Figure 4.12: High speed tracking performance of the SMC. $\psi = 0.1$, $k = 1000$.

which agrees with Khalil's [25, p. 556-557] observation that reducing the boundary layer does not necessarily have a positive effect in the presence of unmodeled dynamics. Lastly, notice how the proposed modified SMC does not suffer nearly as badly from the effects of the unmodeled dynamics - albeit inadvertently.

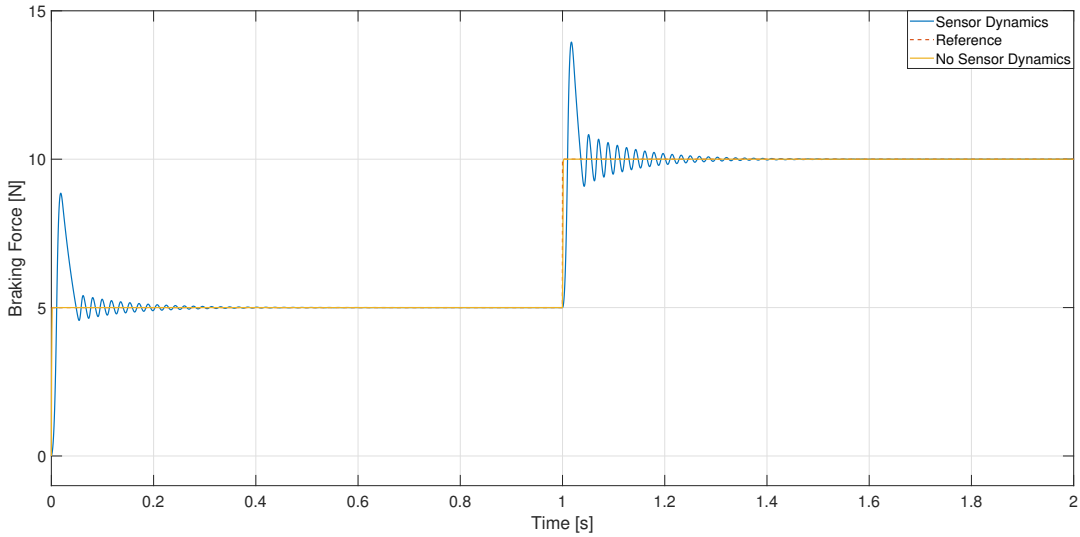

Figure 4.13: Braking force tracking of the traditional first order SMC design, comparing its performance with and without sensor dynamics in the measurement. $\psi = 0.1$, $k = 100$.

4.3 State of the Art

The majority of publications with successful experimental results on the topic of ECB control seem to favor the use of simplistic, linear brake models $F_D \propto v$ - most often based on Wouterse's superconducting ring perspective and kinetic energy dissipation as heat. In general, robust control algorithms are used to compensate for uncertainties in the analytical models - with SMC as a prominent choice [7–9]. Not all publications on ECB control use SMC [10, 11], but some form of adaptive/robust control algorithm is ubiquotous. Even in [11], where 2D FEM was used to analyze the braking force dynamics, required integral action to counter the effect of uncertainties not explained by the finite element analysis.

Lately, detailed parametric analysis of the ECB using 3D FEM [17, 18] seems to have replaced analytical modeling as a combination of technological advancements as well as the models being consistently limited. With the exception of [11], the list of publications where the worlds of parametric analysis and control of ECBs meet with meaningful results is sparse.

Chapter 5

Conclusion

This project report includes an extensive literature review of the theoretical background of eddy current braking, as well as the state of the art within modeling and control of such systems. Digital implementation and comparison of a selection of accepted analytical models and control algorithms has been conducted using MATLAB & Simulink. Additionally, a few "new" perspectives and propositions have been presented:

1. An approximate braking force model including the effects of both high speed demagnetization and magnetic hysteresis.
2. The proposed stationary Linear Quadratic Controller is a solid option given either ideal circumstances or a very accurate model - linear control seems to be feasible.
3. A proposed sliding surface for traditional Sliding Mode Control has been presented and simulated.
4. An empirical modification of the Sliding Mode Control algorithm has been proposed, and it's simulation results shown to outperform the traditional implementation.

Due to the lack of a real world testing rig, the author has not been able to verify the applicability of any of the above propositions.

5.1 Further Work

As mentioned, the few small propositions presented in this document require experimental investigation. A logical next step is therefore either designing and building a testing rig to conduct these experiments, or outsourcing to an existing rig. Possible additions to the discussed control algorithms and models:

1. A more robust LQR may be attainable by adding state augmentation.
2. Continued extension of the braking force model, improving LQR performance.
3. Look into implementation of second order sliding mode control to reduce oscillations and/or chattering. The *Super Twisting Algorithm* is an example of a second order sliding mode control algorithm that warrants investigation.

Bibliography

[1] J.C. Maxwell, "On the induction of electric currents in an infinite plane sheet of uniform conductivity", *Proceedings of the Royal Society of London*, vol. 20, pp. 159–168, 1871 - 1872. DOI: 10.1098/rspl.1871.0038.

[2] R. Rüdenberg, *Energie der Wirbelströme in elektrischen Bremsen und Dynamomaschinen*, ser. Sammlung elektrotechnischer Vorträge. Verlag Enke, Stuttgart, 1906.

[3] W. Zimmermann, "Rechnung und versuch bei der scheibenförmigen wirbelstrombremse", *Archiv für Elektrotechnik*, vol. 10, no. 3-4, pp. 133–154, 1921. DOI: 10.1007/BF01578439.

[4] W. Smythe, "On eddy currents in a rotating disk", *Electrical Engineering*, vol. 61, no. 9, pp. 681–684, 1942. DOI: 10.1109/EE.1942.6436528.

[5] D. Scheiber, "Braking torque on rotating sheet in stationary magnetic field", *The Proceedings of the Institution of Electrical Engineers*, vol. 121, no. 2, pp. 117–122, 1974. DOI: 10.1049/piee.1974.0021.

[6] J. Wouterse, "Critical torque and speed of eddy current brake with widely separated soft iron poles", *IEE Proceedings B (Electric Power Applications)*, vol. 138, no. 4, pp. 153–158, 1991. DOI: 10.1049/ip-b.1991.0019.

[7] K. Lee and K. Park, "Optimal robust control of a contactless brake system using an eddy current", *Mechatronics*, vol. 9, no. 6, pp. 615–631, 1999. DOI: 10.1016/S0957-4158(99)00008-2.

[8] S. Anwar and B. Zheng, "An antilock-braking algorithm for an eddy-current-based brake-by-wire system", *IEEE Transactions on Vehicular Technology*, vol. 56, no. 3, pp. 1100–1107, 2007. DOI: 10.1109/TVT.2007.895604.

[9] J. Song, "Performance evaluation of a hybrid electric brake system with a sliding mode controller", *Mechatronics*, vol. 15, no. 3, pp. 339–358, 2005. DOI: 10.1016/j.mechatronics.2004.09.005.

[10] E. Simeou and D. Georges, "Modeling and control of an eddy current brake", *Control Engineering Practice*, vol. 4, no. 1, pp. 19–26, 1996. DOI: 10.1016/0967-0661(95)00202-4.

[11] R. Hong-Je, K. Jong-Soo, K. Do-Hyun, R. Geun-Hie, K. Yong-Ju, and W. Chung-Yuen, "Design and analysis of an eddy current brake for a high-speed railway train with constant torque control", *Conference Record of the 2000 IEEE Industry Applications Conference*, pp. 277–281, 2000. DOI: 10.1109/IAS.2000.881123.

[12] S. Spurgeon, "Sliding mode control: A tutorial", *2014 European Control Conference (ECC)*, 24 July 2014. DOI: 10.1109/ECC.2014.6862622.

[13] V. Utkin, "Sliding mode control design principles and applications to electric drives", *IEEE Transactions on Industrial Electronics*, vol. 40, no. 1, pp. 23–36, 1993. DOI: 10.1109/41.184818.

[14] L. Davis and J. Reitz, "Eddy currents in finite conducting sheets", *Journal of Applied Physics*, vol. 42, no. 11, pp. 4119–4127, 1971. DOI: 10.1063/1.1659742.

[15] A. Sommerfeld, "Über verzweigte potentiale im raum", *Proceedings of the London Mathematical Society*, vol. 28, pp. 395–429, 1897. DOI: 10.1112/plms/s1-28.1.395.

[16] K. Lee and K. Park, "Modeling eddy currents with boundary conditions by using coulomb's law and the method of images", *IEEE Transactions on Magnetics*, vol. 28, no. 2, pp. 1333–1340, 2002. DOI: 10.1109/20.996020.

[17] S.E. Gay, "Contactless magnetic brake for automotive applications", PhD thesis, A&M University, 2005.

[18] S.E. Gay and M. Ehsani, "Parametric analysis of eddy-current brake performance by 3-d finite-element analysis", *IEEE Transactions on Magnetics*, vol. 42, no. 2, pp. 319–328, 2006. DOI: 10.1109/TMAG.2005.860782.

[19] Colonel W.T. McLyman, *Transformer and Inductor Design Handbook, Third Edition, Revised and Expanded*. Madison Avenue, New York: Marcel Dekker, 2004.

[20] M. Krasnoselskij and A. Pokrovskij, *Systems with hysteresis*. Moscow: Nauka, 1983.

[21] F. Preisach, "Über die magnetische nachwirkung", *Zeitschrift für Physik*, vol. 94, no. 5-6, pp. 277–302, 1935. DOI: 10.1007/BF01349418.

[22] K. Venkataratnam and M. Kadir, "Analysis and performance of eddy-current brakes with ferromagnetic loss drums part 2: Salient-pole brakes", *IEE Proceedings B - Electric Power Applications*, vol. 129, no. 3, pp. 132–142, 1982. DOI: 10.1016/0967-0661(95)00202-4.

[23] B. Anderson and J. Moore, *Linear Optimal Control*. Englewood Cliffs, New Jersey: Prentice-Hall Inc., 1971.

[24] J.E. Slotine and W. Li, *Applied Nonlinear Control*. Englewood Cliffs, New Jersey: Prentice-Hall inc., 1991.

[25] H. Khalil, *Nonlinear Systems, Third Edition*. Englewood Cliffs, New Jersey: Prentice-Hall inc., 2002.